THE JOURNAL OF PHYSICAL CHEMISTRY A
Article
Cite This: J. Phys. Chem. A 2019, 123, 6868−6885
pubs.acs.org/JPCA

Direct Dynamics Simulations of Fragmentation of a Zn(II)-2Cys-2His Oligopeptide. Comparison with Mass Spectrometry Collision-Induced Dissociation

Published as part of The Journal of Physical Chemistry virtual special issue "Hai-Lung Dai Festschrift".

Abdul Malik,[†] Yu-Fu Lin,[‡] Subha Pratihar,[†] Laurence A. Angel,[‡] and William L. Hase*,[†]

[†]Department of Chemistry and Biochemistry, Texas Tech University, Lubbock, Texas 79409-1061 United States
[‡]Department of Chemistry Texas A&M University—Commerce, 2600 South Neal Street, Commerce, Texas 75428, United States

Supporting Information

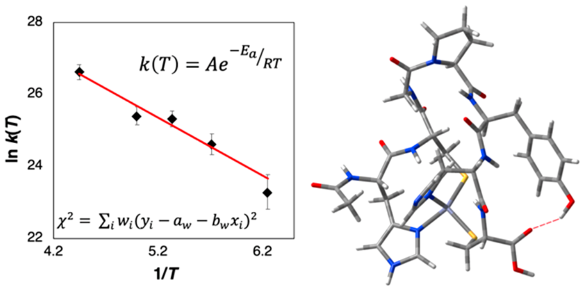

ABSTRACT: Abnormalities in zinc metabolism have been linked to many diseases, including different kinds of cancers and neurological diseases. The present study investigates the fragmentation pathways of a zinc chaperon using a model peptide with the sequence acetyl-His$_1$-Cys$_2$-Gly$_3$-Pro$_4$-Tyr$_5$-His$_6$-Cys$_7$ (analog methanobactin peptide-5, amb$_5$). DFT/M05-2X and B3LYP geometry optimizations of [amb$_5$−3H+Zn(II)]$^-$ predicted three lowest energy conformers with different chelating motifs. Direct dynamics simulations, using the PM7 semiempirical electronic structure method, were performed for these conformers, labeled *a*, *b*, and *c*, to obtain their fragmentation pathways at different temperatures in the range 1600−2250 K. The simulation results were compared with negative ion mode mass spectrometry experiments. For conformer *a*, the number of primary dissociation pathways are 11, 14, 24, 70, and 71 at 1600, 1750, 1875, 2000, and 2250 K, respectively. However, there are only 6, 10, 13, 14, and 19 pathways corresponding to these temperatures that have a probability of 2% or more. For conformer *b*, there are 67 pathways at 2000 K and 71 pathways at 2250 K. For conformer *c*, 17 pathways were observed at 2000 K. For conformer *a*, for two of the most common pathways involving C−C bond dissociation, Arrhenius parameters were calculated. The frequency factors and activation energies are smaller than those for C−C homolytic dissociation in alkanes due to increased stability of the product ions as a result of hydrogen bonding. The activation energies agree with the PM7 barriers for the C−C dissociations. Comparison of the simulation and experimental fragmentation ion yields shows the simulations predict double or triple cleavages of the backbone with Zn(II) retaining its binding sites, whereas the experiment exhibits single cleavages of the backbone accompanied by cleavage of two of the Zn(II) binding sites, resulting in *b*- and *y*-type ions.

I. INTRODUCTION

Being the second most abundant transition metal, Zn(II) plays an important role in biomolecules.[1−3] It is found in about 10% of all human proteins,[2] where it performs two functions. It can either play its role in enzyme catalysis or in the correct folding and stability of zinc finger proteins.[3] To carry out these functions, zinc needs to be transported to different parts of the body. A disruption in this transportation system can cause zinc deficiency which has been linked to many kinds of cancers including prostatic cancer,[4] pancreatic cancer,[5] hepatocellular cancer,[6] and breast cancer,[7] and neurological diseases including Alzheimer's[8−11] and prion disease.[9] Therefore, it is important to investigate potential therapeutics that can treat diseases that result because of abnormal zinc metabolism. Cysteine and histidine have historically been established as two of the most common zinc ion chelators.[12−15]

The model zinc finger oligopeptide, with the sequence acetyl-His$_1$-Cys$_2$-Gly$_3$-Pro$_4$-Tyr$_5$-His$_6$-Cys$_7$ (analog methanobactin peptide-5, amb$_5$), is hexaprotic and will make positively charged ions in acidic pH and negatively charged ions in neutral to basic pH. Determination of which four of these six sites in amb$_5$ deprotonate to bind to Zn(II) may be investigated by ion mobility-mass spectrometry (IM-MS)[16−22] and tandem mass spectrometry (MS/MS)[23−26] experiments. In previous work, Angel et al.[27] analyzed amb$_5$ using IM-MS and MS/MS collision-induced dissociation (CID) and predicted that in basic pH, Zn(II) prefers to bind to 2Cys-2His. This binding behavior of Zn(II) has been well established in solution.[28] It has been reported that cysteine with its thiol group[14] and histidine with its imidazole group[29] bind well with Zn(II) (structure *a* in Figure 1). In addition to these two amino acids, two other competing Zn(II) ligation sites were located by previous work;[27]

Received: May 31, 2019
Revised: July 19, 2019
Published: July 20, 2019

ACS Publications

DOI: 10.1021/acs.jpca.9b05218

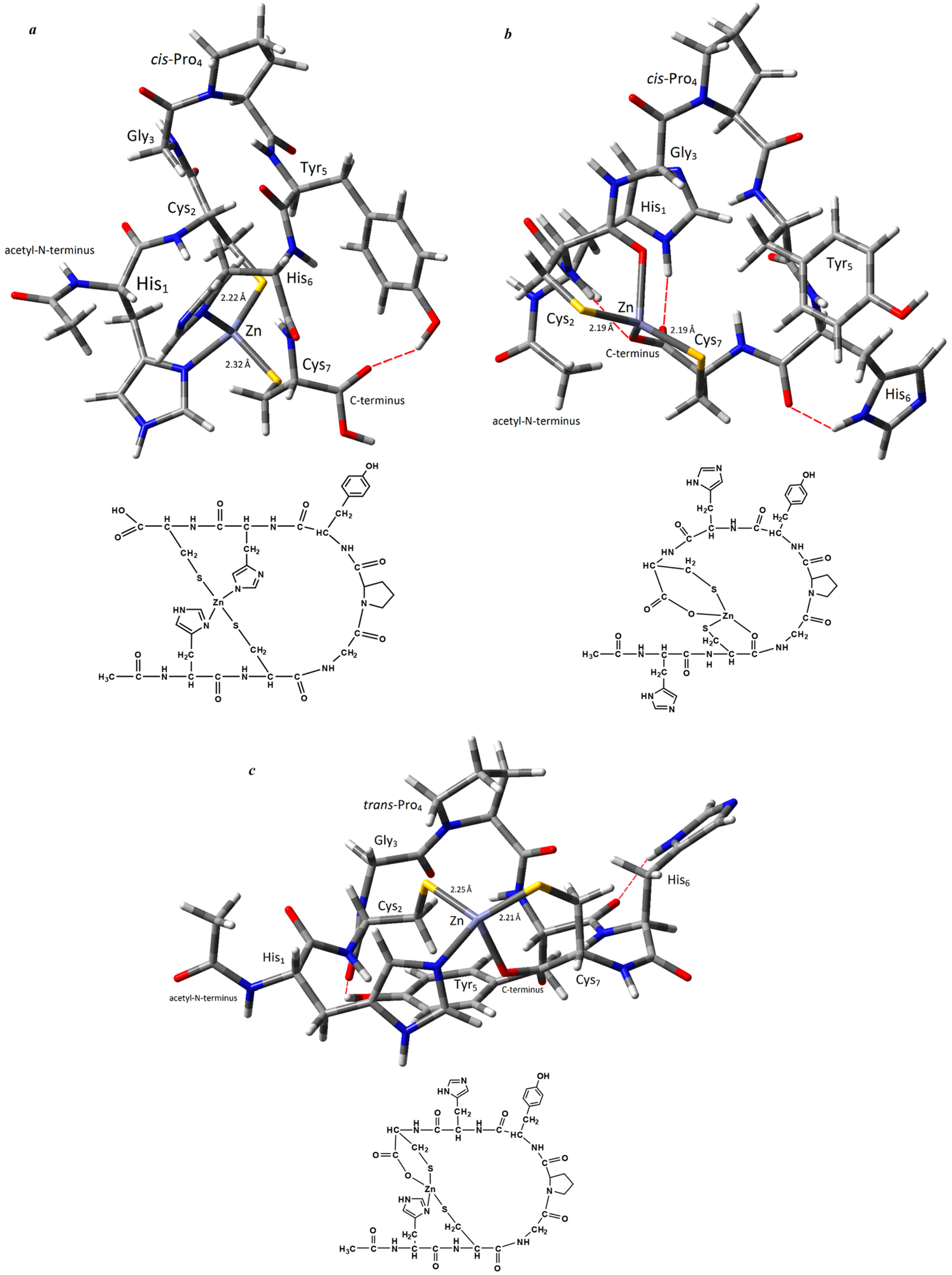

Figure 1. PM7 optimized structures of conformers *a*, *b*, and *c*. 3D structures: gray, C; white, H; red, O; blue, N; yellow, S; and purple, Zn.

the backbone carbonyl group of Cys$_2$ and the carboxylate of the C-terminus (structures *b* and *c* in Figure 1).

For the Angel et al. MS/MS CID experiments[27] (shown in the original article's Supporting Information, with a more comprehensive labeled spectrum shown here in Figure S1), the ions undergo multiple collisions with an inert bath gas and, as described previously,[25] this is expected to lead to excitation of the ions in slight excess of thresholds for their low energy fragmentation pathways. With multiple collisions and each transferring a small amount of energy, the ensuing unimolecular fragmentation dynamics of the ion is expected to be properly understood by assuming statistical unimolecular dynamics.[30] The ions will have a distribution of vibrational energies, $P(E)$, and for each E, the ions are excited by multiple "soft" collisions which are expected to somewhat randomly deposit the collision energy in the ions. Then, with efficient intramolecular vibrational energy redistribution (IVR),[31] the unimolecular dynamics of the ions is in accord with Rice−Ramsperger−Kassel−Marcus (RRKM) theory.[30]

In the present study, electronic structure calculations are used to investigate the ligands that bind to Zn(II) in amb_5 and direct dynamics simulations are performed to study the fragmentation mechanisms of different amb_5 conformers. For the simulations, amb_5 is thermally vibrationally excited to model multiple collision MS/MS CID, as described above. This is a first of its kind study involving Zn(II) and direct dynamics simulations. An important component of the simulations is comparison with experiment. This approach, that is, tying MS/MS with computational methods, is becoming an increasingly important way to explore peptide fragmentation mechanisms.[21,22,32]

II. COMPUTATIONAL METHODOLOGY

II.A. Electronic Structure Theory. Our previous simulations of peptide ion surface-induced dissociation (SID)[33−37] and CID[33,38−42] have used the AM1,[33−35,38] PM3,[36,39,41] and RM1[36−38,40,42] semiempirical electronic structure theories. The accuracy of semiempirical electronic structure theory methods to describe biomolecules containing Zn(II) has been reported by Truhlar et al.[43,44] They developed a database containing geometric parameters and bond dissociation energies calculated using CCSD(T) for model zinc compounds. CCSD(T) is an important method for constructing benchmark databases for small transition metal compounds.[44−46] As compared to CCSD(T), Truhlar et al.[43,44] found M05-2X to be the best DFT functional and PM3 and MNDO/d to be good NDDO semiempirical methods for zinc containing compounds. In this study, PM7[47] predicts the geometry and bond dissociation energies of model zinc compounds better than PM3 or MNDO/d. Bond dissociation energies for Zn(II) model compounds, $[\mathrm{Zn\text{-}SCH_3}]^+$ and $[\mathrm{Zn{-}NH_3}]^{2+}$, were determined using PM7 and compared with other electronic structure theory values. For $[\mathrm{Zn{-}SCH_3}]^+ \rightarrow \mathrm{Zn}^{2+} + \mathrm{SCH_3}^-$ and $[\mathrm{Zn{-}NH_3}]^{2+} \rightarrow \mathrm{Zn}^{2+} + \mathrm{NH_3}$, the respective CCSD(T)[43,44] bond dissociation energies are 433.84 and 134.15 kcal/mol, while the PM7 values are 430.77 and 145.05 kcal/mol. For B3LYP with the LANL2DZ ECP[48,49] for Zn and the 6-31++G basis set for the other atoms, the respective dissociation energies are 414.16 and 134.33 kcal/mol, while with B3LYP and the 6-31G(d) basis set for Zn and 6-31++G for the other atoms the values are 439.29 and 148.48 kcal/mol. PM7 gives an average error of 6.98 kcal/mol as compared with CCSD(T). PM7 reduces the error by 50% as compared to PM3 and MNDO/d, previously considered the best semiempirical methods for Zn(II) compounds.[43,44]

PM7 is used for the direct dynamics simulations reported here and it contains two major corrections over its predecessor PM6. First, it includes improved descriptions of noncovalent interactions (hydrogen bonding and dispersion) based on correction terms proposed in PM6-DH2/PM6-DH+.[47,50] This results in a 70% reduction in error in intermolecular energies as compared to PM6.[47] Second, a modified NDDO formalism was adapted in PM7. The parametrization was performed by keeping in mind its use for biological molecules. It was parametrized by optimizing heats of formation of 4369 compounds and optimizing bond lengths of 5035 compounds. In addition, PM7 gives barrier heights for enzyme catalyzed reactions better than PM6.[47] The use of an ab initio electronic structure method or density functional theory (DFT) is not computationally practical for the direct dynamics simulations reported here.

II.B. Conformers of the $[\mathrm{amb_5{-}3H{+}Zn(II)}]^-$ Complex. The B3LYP//LANL2DZ level of theory containing the Becke three parameter hybrid functionals with the Dunning basis set[51] and effective core potentials (ECPs)[48,49] was used to locate the lowest energy, geometry optimized, gas-phase structures of $[\mathrm{amb_5{-}3H{+}Zn(II)}]^-$. Optimization of the gas-phase structures was based on comparing alternative coordination interactions between the Zn(II) and the sites of the C-terminus, carbonyl groups, and substituent groups of His, Cys, and Tyr. Stability of the complexes was also affected by the type of peptide bonds they contained, that is, cis or trans, and the number of hydrogen bonds. Three of the lowest energy $[\mathrm{amb_5{-}3H{+}Zn(II)}]^-$ complexes located by B3LYP/LANL2DZ were also geometry optimized using MNDO/d, PM7, and M05-2X. The M05-2X calculations used the LANL2DZ ECP for zinc and the 6-311+G(d,p) basis set for the other atoms. Each of these methods found the same three low energy conformers for $[\mathrm{amb_5{-}3H{+}Zn(II)}]^-$ with similar structures for each conformer. The conformers are identified as *a*, *b*, and *c* and their PM7 structures are shown in Figure 1. Conformers *a*, *b*, and *c* are also the lowest free energy conformers found in a comprehensive search of low-energy conformers in ref 27 (see Table S1 of ref 27, where the conformers are identified as Ia, IIa, and IIIa.) However, in future and continuing studies of this project, it would be of interest to perform a molecular dynamics simulation of $[\mathrm{amb_5\text{-}3H{+}Zn(II)}]^-$ and optimize low potential energy structures found in the simulations, to see if there are other low energy conformers.

For all three conformers the coordinating ligands adopted a distorted tetrahedral structure around Zn(II) and included the two thiolate groups of the cysteines. For structure *a*, the other two ligands were the imidazole and imidazolate groups of the two histidines, giving a 2His-2Cys binding motif. For structure *b*, the ligands included two oxygens from the carbonyl group of $\mathrm{Cys_2}$ and the C-terminus carboxylate group. Conformer *c* included the imidazole from $\mathrm{His_1}$ and the oxygen from the C-terminus carboxylate. The energies of the different conformers are given in Table 1. Each electronic structure method identified conformer *b* as the lowest in energy, whose peptide bonds are all trans apart from the *cis*-Gly−Pro bond.

There are several factors that affect the order of electronic stability of the conformers. The Zn−S bond distances are the shortest in *b* with the $\mathrm{Zn{-}Cys_2}$ and $\mathrm{Zn{-}Cys_7}$ bond distances

Table 1. Energies of Different Conformers of $[\mathrm{amb_5{-}3H{+}Zn(II)}]^-$

	energy[b]			
conformer[a]	MNDO/d	PM7	M05-2X[c]	B3LYP[d]
a	9.97	14.25	31.02	44.19
b	0	0	0	0
c	16.9	18.57	26.76	32.91

[a] Structures of the conformers are in Figure 1. [b] Energies are in kcal/mol. [c] The calculation used the LANL2DZ effective core potential for zinc and 6-311+G(d,p) basis set for the other atoms. [d] The calculations used LANL2DZ for all the atoms.

both 2.19 Å, whereas, in *a*, they are 2.24 and 2.32 Å, and in *c*, they are 2.25 and 2.20 Å, respectively. The smaller Zn−S bond distances in *b* also correlates to generally smaller Mulliken charges on the sulfur atoms and Zn(II), as compared to the other conformers (Table 2), showing the thiolate groups are dispersing the positive charge of Zn(II) more effectively in conformer *b*. The Zn−N bond lengths in *a* are 1.97 and 2.11 Å and in *c* 2.10 Å. The carboxylic acid on the C-terminus[27] has the lowest pK_a among the six hexaprotic sites that are competing for Zn(II) ligation in this model peptide. This favors deprotonation of the C-terminus as in structure *b* as compared to N in the imidazole ring for conformer *a*. Lessened steric strain for *b* as compared to *a* could also be contributing to the lower energy because the thiolate and oxygen ligands of *b* coordinate the Zn(II) ion further from the ideal tetrahedral geometry than the ligands of *a* or *c*. Both conformers *a* and *b* contain the *cis*-Gly-Pro peptide bond, which is common in peptides and proteins.[20,52−54] Conformer *c* has two nonproline cis peptide bonds: *cis*-Cys_2-Gly_3 and *cis*-His_6-Cys_7.[55−58]

Table 2. Comparison of Mulliken Charges on Selected Atoms in Conformers *a*, *b*, and *c*

	Mulliken charges on selected atoms		
atoms	*a*	*b*	*c*
Zn(II)	1.26	1.24	1.25
His_1-N	*−0.48*[a]	−0.56	*−0.47*
Cys_2-S	*−0.73*	*−0.71*	*−0.77*
Cys_2-O	−0.54	*−0.58*	−0.61
His_6-N	*−0.64*	−0.53	−0.53
Cys_7-S	*−0.8*	*−0.75*	*−0.74*
C-terminus-O	−0.62	*−0.77*	*−0.7*

[a] Italicized numbers refer to the sites chelating the Zn(II).

Figure 1 also indicates the number of hydrogen bonds in each conformer. Conformer *a* exhibits a hydrogen bond between the hydroxyl group of Tyr and the carboxylate of the C-terminus. Conformer *b* has hydrogen bonds between the imidazole group of His_1 and the carboxylate of the C-terminus, the imidazole group of His_6 and carbonyl group of Cys_7, and the amine group of Cys_2 and the Zn bound oxygen of the carboxylate C-terminus. Conformer *c* exhibits two hydrogen bonds between the imidazole group of His_6 and the carbonyl group of Tyr_5, and the hydroxyl group of Tyr_5 and carbonyl group of Cys_2.

X-ray crystallographic studies have determined bond distances and angles of the coordination center of zinc finger proteins[59,60] and show three types of coordination, that is, 2His-2Cys, His-3Cys, and 4Cys, with 2His-2Cys being the most common.[60] Carmay et al.[59] reported the mean and standard deviations of the zinc coordination center by averaging over the three 2His-2Cys zinc binding domains from the X-ray structure of the Zif268 protein−DNA complex from PDB entry 1AAY.[61] They found that the angles of S−Zn−S and N−Zn−N were 117° ± 6 and 105° ± 6, respectively, whereas the Zn−S and Zn−N bond distances were 2.29 ± 0.10 Å and 2.04 ± 0.08 Å, respectively. The Zn−S and Zn−N bond distances predicted by PM7 for all three conformers are within one standard deviation to those found in the crystal structure. Table 3 shows all the PM7 bond angles for tetra-coordinated zinc in the three conformers studied here and the S−Zn−S bond angles are also within one standard deviation for conformers *a* and *c* whereas for *b* the 133.46° is outside the range. The N−Zn−N bond angle in conformer *a* is smaller than predicted by X-ray structure.

The X-ray study reports angles measured from a crystallized zinc finger protein−DNA complex, while the current study compares this structure with a small oligopeptide bound to Zn(II). Solvation in the crystallization should not have a significant effect on the structure and our previous research on molecular modeling of Zn(II)-bound oligopeptides showed including an aqueous solvent model produced essentially the same structures as the gas-phase method.[16,27] However, there is a possibility that another low-energy conformer exists.

II.C. Direct Dynamics Simulations. PM7 direct dynamics simulations were performed with a VENUS/MOPAC software package, in which the VENUS chemical dynamics computer program[62,63] is interfaced with the MOPAC electronic structure computer program.[64] For the CID experiments, with which the simulations are compared, the negatively charged $[amb_5{-}3H{+}Zn(II)]^-$ ion undergoes about 700 collisions with neutral argon atoms before it fragments. As discussed in the Introduction, such multiple collisions are expected to result in statistical activation of the ion. For the direct dynamics simulations reported here, statistical thermal activation of the ion was considered.

The unimolecular dissociation dynamics of conformers *a*, *b*, and *c* of the $[amb_5{-}3H{+}Zn(II)]^-$ ion were studied by direct dynamics simulations. The $s = 306$ vibrational modes of these ions were randomly excited using classical microcanonical normal mode sampling.[65] The vibrational energy E for the excitation is assigned a temperature using $E = sk_BT$. Temperatures ranging from 1600 to 2250 K were considered and the ion's vibrational energy E, for temperatures of 1600, 1750, 1875, 2000, and 2250 K, equals 969, 1060, 1136, 1211, and 1363 kcal/mol, respectively. The rotational energy of the ion was sampled for a Boltzmann distribution at 300 K. The zero-point energy of the ion was not included in its initial classical energy.

More than 5000 trajectories were calculated for conformers *a*, *b*, and *c*. For temperatures 1600, 1750, 1875, 2000, and 2250 K, the simulations were run for 30, 20, 20, 10, and 7 ps, respectively. Different integration step sizes and the two integration algorithms, velocity-Verlet[66] and sixth-order symplectic,[67,68] were tested. For 1600 K, the velocity-Verlet algorithm was used

Table 3. Comparison of PM7 Optimized Geometry Around Tetra-Coordinated Zn(II)

comparison of geometries of all three conformers					
a	angle (deg)	*b*	angle (deg)	*c*	angle (deg)
(His_1-N)-Zn-(Cys_2-S)	126.99	(Cys_2-O)-Zn-(Cys_2-S)	89.62	(His_1-N)-Zn-(Cys_2-S)	95.09
(His_1-N)-Zn-(Cys_7-S)	100.43	(Cys_2-O)-Zn-(Cys_7-S)	116.60	(His_1-N)-Zn-(Cys_7-S)	134.81
(His_6-N)-Zn-(Cys_2-S)	113.35	(Cterm-O)-Zn-(Cys_2-S)	122.24	(Cterm-O)-Zn-(Cys_2-S)	118.30
(His_6-N)-Zn-(Cys_7-S)	105.63	(Cterm-O)-Zn-(Cys_7-S)	98.00	(Cterm-O)-Zn-(Cys_7-S)	100.99
(Cys_2-S)-Zn-(Cys_7-S)	112.60	(Cys_2-S)-Zn-(Cys_7-S)	133.46	(Cys_2-S)-Zn-(Cys_7-S)	120.10
(His_1-N)-Zn-(His_6-S)	94.82	(Cterm-O)-Zn-(Cys_2-O)	87.51	(Cterm-O)-Zn-(His_1-N)	82.51

DOI: 10.1021/acs.jpca.9b05218
J. Phys. Chem. A 2019, 123, 6868−6885

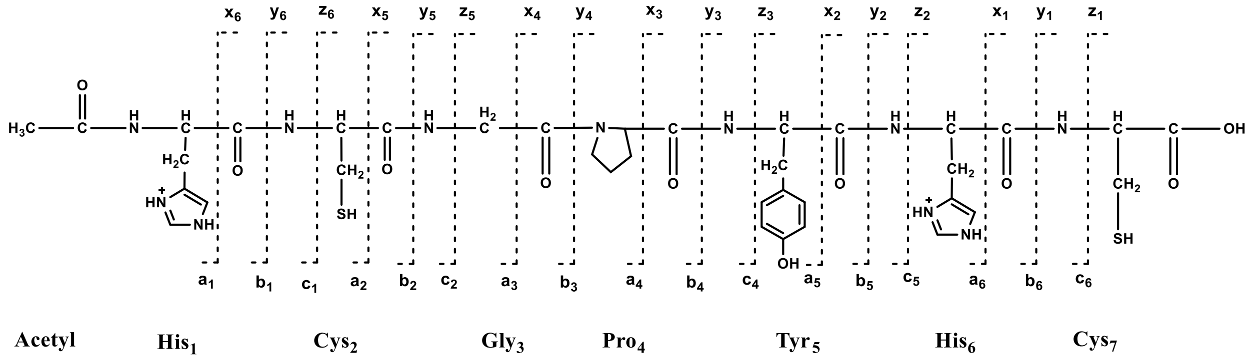

Figure 2. Primary structure of amb$_5$ without Zn(II) and abbreviation used to characterize the fragments.[81]

to integrate Newton's equations, with a 0.005 fs time step, and gave energy conservation to within 10% for up to 30 ps. For the higher temperatures, Hamilton's equations of motion were integrated, using a sixth-order symplectic algorithm and a 0.01 fs time, resulting in energy conservation to within 10% for 20 ps.

During a few trajectories of conformer *a*, zinc made a bond with the C-terminus oxygen or Cys$_2$ oxygen (similar to conformer *b*). But no complete interconversion of any of the conformers was observed.

II.D. Analyses of the Trajectory Results. Each trajectory was animated to determine the time at which it fragmented and its fragmentation mechanism. For each ion structure and simulation temperature, intramolecular vibrational energy redistribution (IVR)[69−73] was faster than the dissociation rate, resulting in Rice−Ramsperger−Kassel−Marcus (RRKM)[73] kinetics, and, thus, unimolecular rate constants could be determined from the simulation results. The total rate constant $k(T)$ for unimolecular decomposition of the ion, for each ion conformer and temperature, was determined by plotting[74]

$$N(t)/N(0) = \exp(-k(T)t) \tag{1}$$

where $N(0)$ is the total number of trajectories at $t = 0$ and $N(t)$ is the number of undissociated trajectories at t. The uncertainty reported for $k(T)$, $\Delta k(T)$, is for a 95% confidence interval.[75]

This $k(T)$ is the sum of rate constants for the individual pathways $k_i(T)$

$$k(T) = \sum_i k_i(T) \tag{2}$$

where $k_i(T) = p_i k(T)$ and p_i is the fraction of the ith pathway out of the total number of pathways. The $k_i(T)$ include the full anharmonicity of the potential energy surface used for the direct dynamics simulation. With uncertainties, $[k_i(T) \pm \Delta k_i(T)] = [p_i \pm \Delta p_i][k(T) \pm \Delta k(T)]$, where $\Delta k_i(T) = [\Delta p_i + \Delta k(T)]$. Since $\Delta k(T) \gg \Delta p_i$, $\Delta k_i(T) \approx \Delta k(T)$.

For a molecule with a large number of normal modes s such that $s \approx s - 1$, the classical Rice−Ramsperger−Kassel−Marcus (RRKM) rate constant $k(E)$ becomes equivalent to the classical transition state theory (TST) rate constant $k(T)$ if $E_o/E \ll 1$, where E_o is the unimolecular dissociation energy.[76] Both of these criteria are met for the simulations performed here. The rate constant for an individual dissociation pathway may be represented by the Arrhenius equation, that is, $k_i(T) = A_i \exp(-E_{a,i}/k_BT)$. The Arrhenius activation energy $E_{a,i}$ is the classical dissociation energy E_o[77] and may be compared to the value given by the PM7 method used for the simulations. In previous work, Arrhenius parameters have been derived from $k_i(T)$ determined from direct dynamics simulations[38,74] and from chemical dynamics simulations with analytic potentials.[31,78] Given the interaction between Zn(II) and the π electrons of the Tyr side group, anharmonicity[31] may play an important role in the thermal unimolecular dissociation of $[\text{amb}_5{-}3\text{H}{+}\text{Zn(II)}]^-$ and is included in the $k_i(T)$ determined from the current simulations. In determining Arrhenius parameters for $k(T)$ and $k_i(T)$, the uncertainties $\Delta k(T)$ and $\Delta k_i(T)$ were included for weighted linear regression fits[79,80] to natural logarithms of the rate constants versus T^{-1}.

III. SIMULATION RESULTS

III.A. Dissociation Pathways and Their Probabilities.

The fragmentation dynamics of structures *a* and *b* were studied in detail. For structure *a*, trajectories were calculated at 1600, 1750, 1875, 2000, and 2250 K. For structure *b*, the calculations were for 2000 and 2250 K. For temperatures lower than 1600 K, no fragmentation was observed in the simulations for both structures, even after several picoseconds. For both *a* and *b*, 300 trajectories were run at each temperature. Results are also reported for 100 trajectories at 2000 K for structure *c*. In the work presented here only primary dissociation events of $[\text{amb}_5{-}3\text{H}{+}\text{Zn(II)}]^-$ are considered. Secondary dissociations of the primary dissociation fragments will be considered in future studies.

The common nomenclature used to represent protein fragments in mass spectrometry is shown in Figure 2.[81] The number of fragmentation pathways, number of ions formed, and the number of ions formed with a percentage of 1% or greater, with respect to the total number of ions formed, are given in Table 4 for the simulations of conformers *a*, *b*, and *c*. Each pathway leads to a unique ion, so that the number of ions equals the number of pathways. The number of pathways for conformer *a* increases with temperature. For conformer *a*, there is a striking increase in the number of fragment ions upon increasing the temperature from 1875 to 2000 K. For both conformers *a* and *b* the number of pathways are similar for 2000 and 2250 K, with both conformers having nearly the same number of pathways. The number of pathways is much smaller for conformer *c*. Though the number of ions increases substantially with increase in temperature for conformer *a*, if only ions with a probability of 1% or more with respect to the total number of ions are considered, the number of ions is substantially smaller for 2000 and 2250 K. For the lower temperatures of 1600, 1750, and 1875 K, each ion has a probability greater than 1%. With this 1% constraint, the number of ions for conformer *a* is 11, 14, 24, 26, and 19 for 1600, 1750, 1875, 2000, and 2250 K, respectively. For conformer *b* at 2000 and 2250 K temperatures, the effect of this 1% constraint is similar to that for conformer *a*. For conformer *c*

DOI: 10.1021/acs.jpca.9b05218
J. Phys. Chem. A 2019, 123, 6868−6885

Table 4. Number of Fragmentation Pathways and Ions

T (K)	no. pathways	no. ions	no. ions > 1%[a]
	conformer *a*		
1600	11	11	11 (6)
1750	14	14	14 (10)
1875	24	24	24 (13)
2000	70	70	26 (14)
2250	71	71	19 (19)
	conformer *b*		
2000	67	67	18 (12)
2250	71	71	24 (15)
	conformer *c*		
2000	17	17	17 (4)

[a] Number of ions having greater than 1% of the total ion yield. In parentheses is the number of ions having greater than 2% of the total ion yield.

Table 6. Percentage Probabilities of Conformers *b* and *c* Dissociation Pathways versus Temperature

	temperature (K)		
	conformer *b*		conformer *c*
pathway	2000	2250	2000
NR[a]	38.0	34.5	72.0
1	5.0 (8.1)[b]	5.0 (7.7)	6.0 (20.7)
2	2.0 (3.2)	1.5 (2.3)	0.0 (0.0)
3	0.5 (0.8)	1.5 (2.3)	5.0 (17.2)
4	6.0 (9.7)	6.0 (9.2)	2.0 (6.9)
5	3.0 (4.8)	1.5 (2.3)	0.0 (0.0)
6	1.5 (2.4)	1.0 (1.5)	3.0 (10.3)
7	1.5 (2.4)	0.5 (0.8)	0.0 (0.0)
8	1.5 (2.4)	1.0 (0.5)	1.0 (3.4)
9	2.0 (3.2)	2.5 (3.8)	1.0 (3.4)
10	0.0 (0.0)	0.0 (0.0)	0.0 (0.0)
OP[c]	39.0 (62.9)	44.5 (68.5)	10.0 (37.9)

[a] No reaction. [b] In parentheses is the probability of dissociation out of the total number of reactive trajectories. [c] Other paths.

at 2000 K, the yield of each ion is greater than the 1% constraint. In previous simulations,[38,40] ions with a yield greater than 2% were considered for comparison with experiment. For the current study, the number of ions with a yield greater than 2% is given in parentheses in Table 4. All of the ions formed for conformers *a*, *b*, and *c* for all of the temperatures are listed in Tables S2−S9.

The probabilities of the first ten pathways are given in Table 5 for conformer *a* and in Table 6 for conformers *b* and *c*. For conformer *a*, the percentage of the trajectories which fragment increases with temperature and is 5%, 20%, 45%, 71%, and 91% for 1600, 1750, 1875, 2000, and 2250 K, respectively. The fragmentation percentage is higher for conformer *a* than *b*, particularly at 2250 K. Conformer *c* has a fragmentation percentage substantially smaller than for conformers *a* and *b*. For conformer *a*, atomistic mechanisms for pathways 1−4 are given in Figure 3, for pathways 5−8 in Figure 4, and pathways 9 and 10, in Figure 5. Included with the mechanisms are *m*/*z* values for the product ions. Mechanisms for pathways 11−15 for conformer *a* are shown in Figure S2.

In analyzing the mechanisms, there are dynamical features common to all the mechanisms and each of the conformers. For most of the pathways, more than one bond was broken to generate fragments. As suggested before,[27] with 2Cys-2His as ligands, Zn(II) gives a more stable distorted trigonal planar geometry binding with δN of His$_1$ and two sulfurs of 2Cys as compared to the tetra-coordinated complex. In most of the conformer *a* trajectories at each temperature, the N(His$_1$)−Zn bond readily breaks within femtoseconds generating a tricoordinated Zn(II) complex. Many of the fragmentation pathways ensue from this complex. The Zn−O(Cys$_2$) bond in structure *b* also ruptured forming a tricoordinated Zn(II) complex, leading to multiple fragmentation pathways. Regardless of the fragmentation pathway for conformer *a*, one of the two Zn−S bonds broke in 33.6% of the trajectories.

In the following, fragmentation pathways 1−10 in Figures 3−5 are discussed. Though the fragmentations in these figures are for conformer *a*, conformers *b* and *c* have similar fragmentation mechanisms, forming the same ions. The important pathway 1 involves homolytic dissociation of a C−C bond and breaking of a Zn−N bond, generating a tricoordinated Zn(II) complex. For this pathway an ion with *m*/*z* 766.1 is formed, for fragment $[x_6\text{+Zn(II)}]^-$. This *m*/*z*, seen for conformers *a*, *b*, and *c*, was not prominent in the experimental spectrum. For the experimental excitation energies, the $[x_6\text{+Zn(II)}]^-$ ion may further dissociate.[82] A likely secondary dissociation is loss of CO from x_6 to give the $[y_6\text{+Zn(II)}]^-$ ion with *m*/*z* 738.1, found in the experimental spectrum at *m*/*z* 739.1 and shown in Figure 4 as pathway 5. This

Table 5. Percentage Probabilities of Conformer *a* Dissociation Pathways versus Temperature

	temperature (K)				
pathway	1600	1750	1875	2000	2250
NR[a]	95.11	79.6	55.0	28.5	9.0
1	1.6 (31.8)[b]	8.4 (41.2)	5.5 (12.2)	6.0 (8.4)	1.0 (1.1)
2	0.2 (4.5)	1.6 (7.8)	7.5 (16.7)	3.5 (4.9)	2.0 (2.2)
3	0.4 (9.1)	2.0 (9.8)	1.5 (3.3)	2.5 (3.5)	1.0 (1.1)
4	0.0 (0.0)	1.6 (7.8)	3.0 (6.7)	1.0 (1.4)	2.0 (2.2)
5	0.0 (0.0)	0.0 (0.0)	0.0 (0.0)	2.5 (3.5)	2.0 (2.2)
6	0.2 (4.5)	0.8 (3.9)	3.5 (7.8)	6.0 (8.4)	5.0 (5.5)
7	0.2 (4.5)	0.8 (3.9)	1.5 (3.3)	0.5 (0.7)	3.0 (3.3)
8	0.0 (0.0)	1.6 (7.8)	1.5 (3.3)	1.5 (2.1)	1.0 (1.1)
9	0.7 (13.6)	0.8 (3.9)	4.5 (10.0)	1.0 (1.4)	3.0 (3.3)
10	0.0 (0.0)	0.0 (0.0)	1.5 (3.3)	0.5 (0.7)	2.0 (2.2)
OP[c]	1.6 (32)	2.8 (13.9)	15.0 (33.4)	46.5 (65.0)	69.0 (75.8)

[a] No reaction. [b] In parentheses is the probability of dissociation out of the total number of reactive trajectories. [c] Other paths.

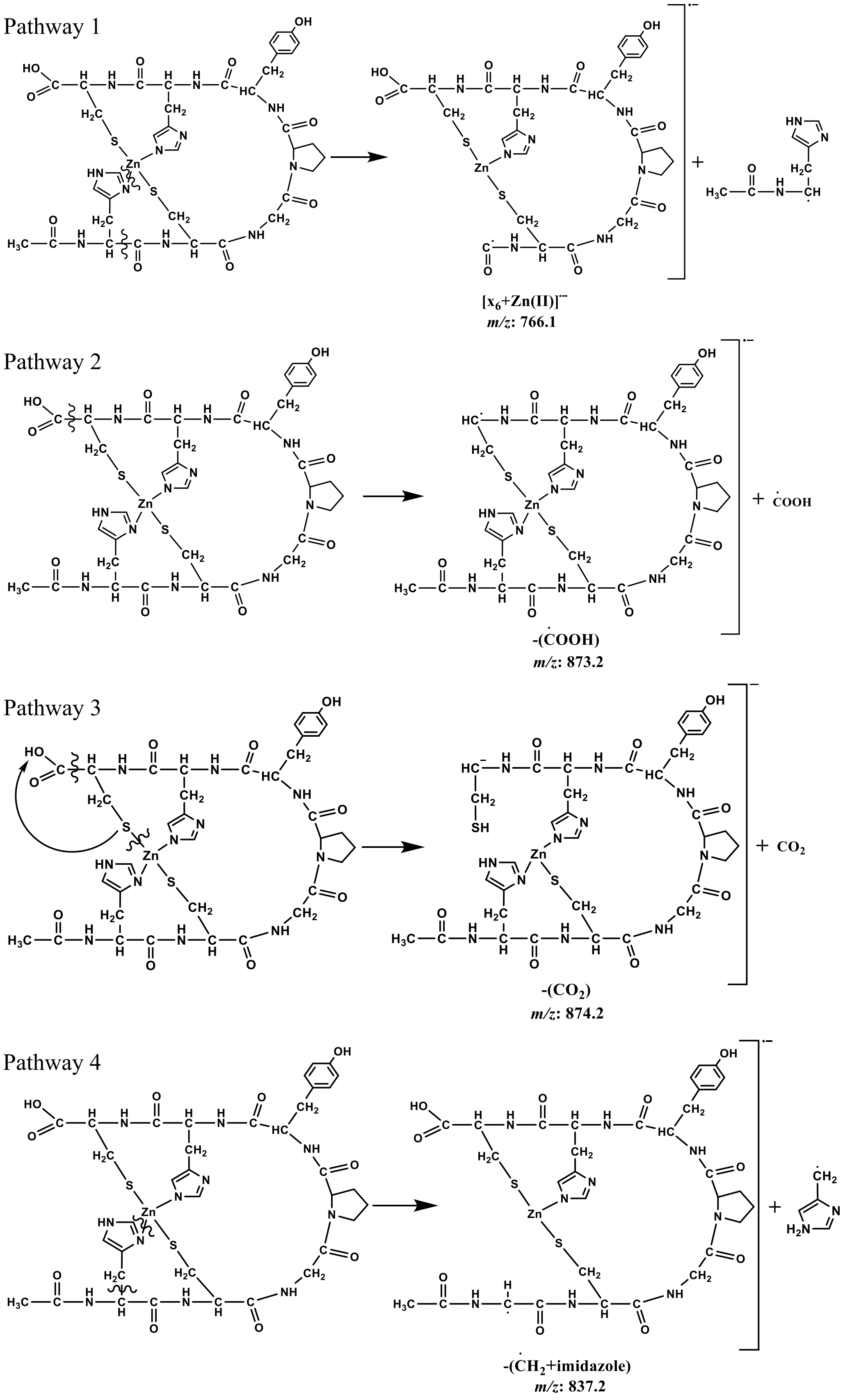

Figure 3. Mechanisms for dissociation pathways 1−4 for conformer *a*.

indicates that, if the ion *m*/*z* 766.1 is formed in the experiment, it dissociates. Pathway 2 is a homolytic C−C dissociation and involves loss of the carboxylic acid group on the C-terminus. The ion with *m*/*z* 873.2, formed by this pathway, was observed for

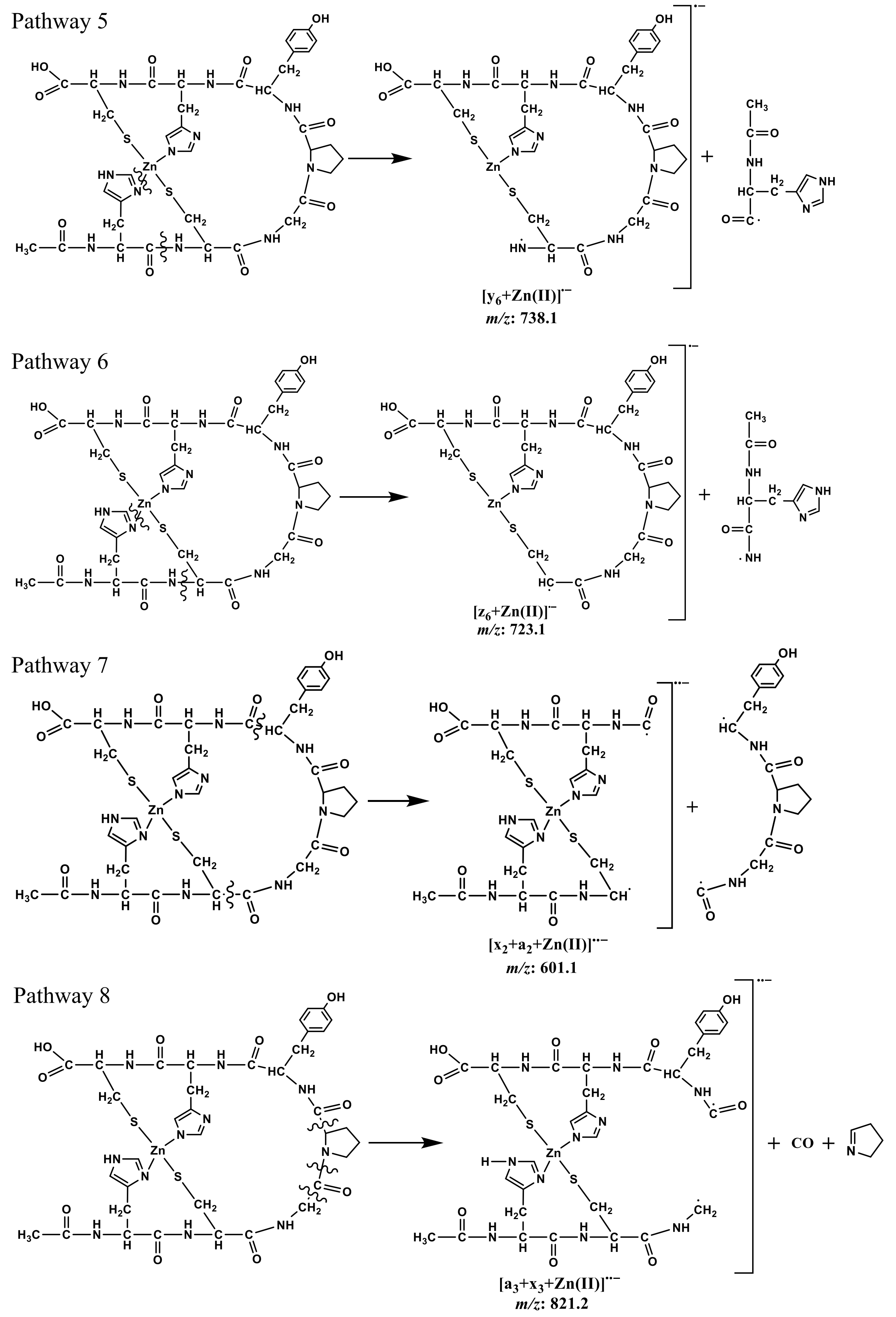

Figure 4. Mechanisms for dissociation pathways 5−8 for conformer *a*.

conformers *a* and *b*. Pathway 3 is a concerted reaction involving proton transfer and C−C bond cleavage. The reaction starts when the most acidic proton in the system (hydrogen of terminal carboxylic acid group) comes in vicinity of one of the

DOI: 10.1021/acs.jpca.9b05218
J. Phys. Chem. A 2019, 123, 6868−6885

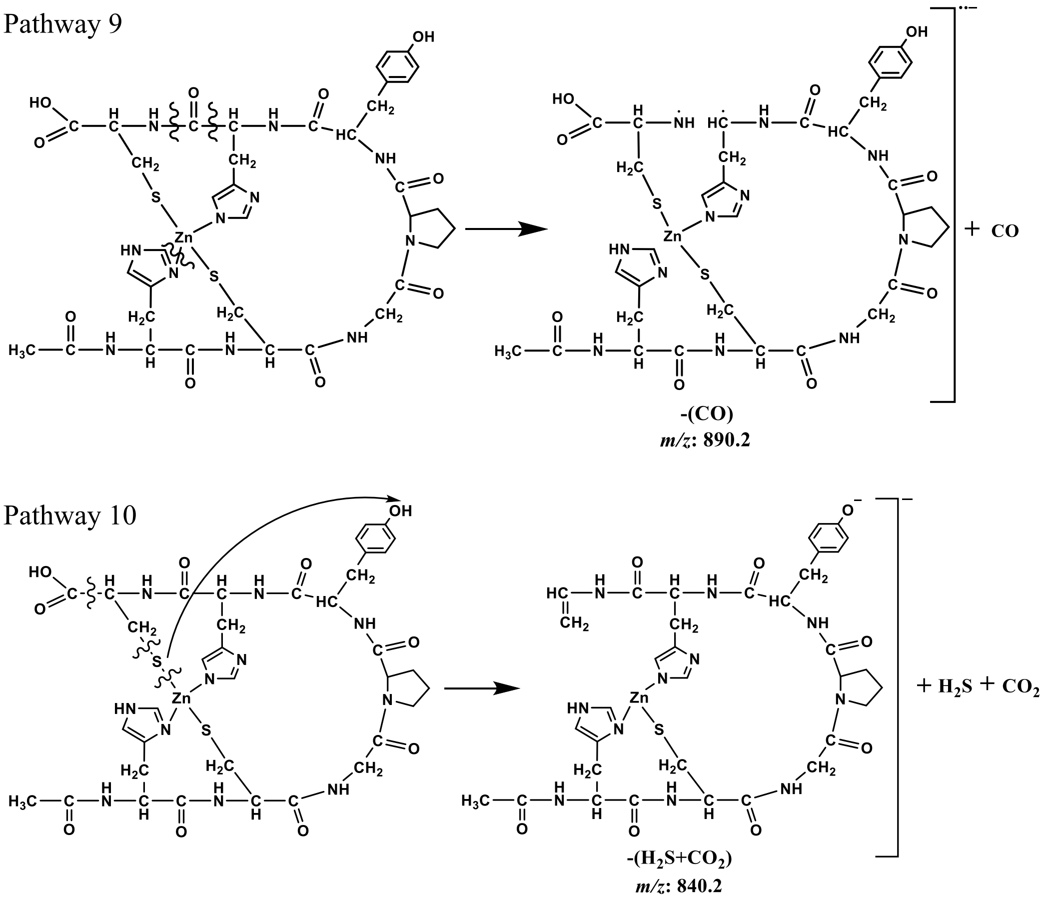

Figure 5. Mechanisms for dissociation pathways 9−10 for conformer *a*.

thiol groups. Sulfur plucks this proton, breaking its bond with Zn(II). This is followed promptly by C−C bond cleavage generating CO_2 and a large ion with *m*/*z* 874.2. This *m*/*z* is observed for all three conformers and in the experiments.

Pathway 4 is the loss of a (CH_2+imi), where imi stands for the imidazole group, leaving behind the fragment with *m*/*z* 837.2. This *m*/*z* is present for all three conformers. Pathway 5 involves breaking the amide and Zn−N bonds of His_1 resulting in a fragment with *m*/*z* 738.1. This is the same species as that for pathway 1, with the additional loss of CO, that is, $[y_6\text{+Zn(II)}]^-$, and is present in the experiments and for conformers *a* and *b*. Pathway 6 is observed for all three conformers with fragment $[z_6\text{+Zn(II)}]^-$ and *m*/*z* 723.1 but is not prominent in the experiments. Pathway 7, found for both conformers *a* and *b*, gives the $[a_2+x_2\text{+Zn(II)}]^-$ fragment with *m*/*z* 601.1. Pathway 8 is the loss of CO and an azoline ring (minus H^+) giving a fragment with *m*/*z* 821.2, found for all three conformers. Pathway 9 is one of the most common pathways. It involves the loss of any one of the CO molecules, resulting in *m*/*z* 890.2. Pathway 10 is the loss of (H_2S+CO_2) giving a negatively charged fragment with *m*/*z* 840.2. Pathways 11−15, Figure S2, give fragment ions with *m*/*z* 770.2 (769.2) for $[a_6\text{+Zn(II)}]^-$, 658.1 for $[b_3+y_2\text{+Zn(II)}]^-$ or $[a_3+x_2\text{+Zn(II)}]^-$, 678.1 (677.1) for $[c_5\text{+Zn(II)}]^-$, 730.1 for −($2CH_2$+PhOH+imi) and 636.1 for $[y_5\text{+Zn(II)}]^-$ or $[y_6\text{+Zn(II)}-(\text{CONHCH}_2\text{+COOH})]^-$, respectively. For three of these, the same product types, that is, $[a_6\text{+Zn(II)}]^-$, $[c_5\text{+Zn(II)}]^-$, and $[y_5\text{+Zn(II)}]^-$ were observed experimentally and their *m*/*z* values are in parentheses. Pathway 12 with ion *m*/*z* 658.1 is an important pathway for conformer *a* at temperatures 2000 and 2250 K with two channels, namely, $[b_3+y_2\text{+Zn(II)}]^-$ and $[a_3+x_2\text{+Zn(II)}]^-$. Pathway 14 with ion *m*/*z* 730.1 shows the loss of two side groups and explains the abbreviations used to label complex dissociation fragments.

For 1600, 1750, and 1875 K more than 50% of the trajectories for conformer *a* are nonreactive. More reaction is expected at these temperatures, if the trajectories were integrated for more than 20−30 ps. This is particularly the case at 1600 K, where 95% of the trajectories are nonreactive. At 1600 K, proton transfer without fragmentation is the most common phenomenon but is not identified as a pathway since this does not generate fragment ions. As the temperature is increased, proton transfer is followed by fragmentation.

III.B. Fragmentation Ions and Their Probability Distributions. Ions observed for fragmentation of conformer *a* are listed in Table 7. Relative probabilities for formation of these ions are listed in Table 8. Following previous work[38,40] and for comparison with experiment, only ions with more than 2% of the total yield are included. All of the ions are listed in the Tables S2−S6. For 1600 and 1750 K, the dominant ion is $[x_6\text{+Zn(II)}]^-$ with *m*/*z* 766.1, resulting from pathway 1. For 1750 K there are four ions with a probability 20−25% of that for this dominant ion. However, for 1600 K, ions resulting from loss of CO with *m*/*z* 890.2, pathway 9, loss of CONH with *m*/*z* 875.2, loss of CO_2 with *m*/*z* 874.2, pathway 3 and loss of $COCH_3$ with *m*/*z* 875.2 are quite important, with the first two having probabilities of ∼45% and later two with probabilities of ∼30% with respect to $[x_6\text{+Zn(II)}]^-$. Upon raising the temperature to 1875 K there are seven ions that have a probability greater than 30% with respect to the most occurring pathway. The dominant ion is now

Table 7. Fragment Ions for Conformer *a*[a]

m/*z*	fragment
916.2	$-(H_2)$
900.2	$-(H_2O)$
890.2	−(CO)
875.2[b]	−(CONH)
875.2[c]	$-(COCH_3)$
874.2	$-(CO_2)$
873.2	−(COOH)
872.2	$-(CO+H_2O)$
861.2	$[a_2+x_4+Zn(II)]^-$
840.2	$-(SCO+H_2O)$ or $-(CO_2+H_2S)$
837.2	$-(CH_2+imi)$
821.2	$[a_3+x_3+Zn(II)]^-$
811.2	$-(CH_2+PhOH)$
766.1	$[x_6+Zn(II)]^-$
764.1	$[a_2+x_3+Zn(II)]^-$ or $[c_2+z_3+Zn(II)]^-$
755.2	$[a_4+x_2+Zn(II)]^-$
738.1	$[y_6+Zn(II)]^-$ or $[x_6+Zn(II)\text{-}(CO)]^-$
727.1	$[a_4+y_2+Zn(II)]^-$
723.1	$[z_6+Zn(II)]^-$
707.1	$[a_3+x_3-x_1+SH+Zn(II)]^-$
693.1	$[y_6+Zn(II)-(COOH)]^-$
681.1	$[y_6+Zn(II)-(CO+CH_2NH)]^-$
678.1	$[z_6+Zn(II)-(COOH)]^-$ or $[c_5+Zn(II)]^-$
664.1	$[x_5+Zn(II)]^-$
658.1	$[b_3+y_2+Zn(II)]^-$ or $[a_3+x_2+Zn(II)]^-$
636.1	$[y_5+Zn(II)]^-$ or $[y_6+Zn(II)-(CONHCH_2+COOH)]^-$
601.1	$[a_2+x_2+Zn(II)]^-$
587.1	$[a_3+y_2+Zn(II)-(CONH)]^-$
558.1	$[a_2+z_2+Zn(II)]^-$
541.1	$[z_3+NHC_2H_3S+Zn(II)]^-$
421.0	$[a_3+CH_2S+Zn(II)]^-$
393.1	$[y_2+CH_2S+Zn(II)]^-$

[a]Only ions with a yield greater than 2% are listed. [b]Loss of (CONH). [c]Loss of $(COCH_3)$.

m/*z* 873.2, for pathway 2 and elimination of COOH, with the ion *m*/*z* 766.1 the second most important.

For fragmentation of conformer *a* at 2000 K, ions *m*/*z* 723.1 and *m*/*z* 766.1, for pathways 6 and 1, are the most dominant with equal probabilities, while *m*/*z* 873.2 for pathway 2 and *m*/*z* 658.1 for pathway 12, shown in Figure S2, are the next two most important ions. At this temperature seven ions are formed with a probability 30% or greater than that for the two dominant ions. For 2250 K, pathway 6 forming *m*/*z* 723.1 is dominant. Ion *m*/*z* 766.1 is barely observed, since at this high temperature the $[x_6+Zn(II)]^-$ ion releases either an additional CO or CONH, forming a fragment with y_6 or z_6 instead of x_6. At 2250 K, 17 ions are formed with a probability 30% or greater than that for the dominant *m*/*z* 723.1 ion. For the higher temperatures of 2000 and 2250 K, pathways involving loss of smaller fragments as CO, CO_2, H_2O, CONH, and COOH become important.

Relative probabilities of ions formed by fragmentations of conformers *b* and *c* are listed in Table 9. For conformer *b* the results are for simulation temperatures of 2000 and 2250 K, while for conformer *c* for a temperature of 2000 K. As for conformer *a*, only ions with more than 2% of the total yield are included. Comparison of the ion probabilities in Tables 8 and 9, for conformers *a* and *b* at 2000 and 2250 K, shows there are similarities in the ion distributions for these two conformers. In particular for the pathways resulting in the loss of small molecules as described above for conformer *a*. The fragmentation pattern for conformer *c* in Table 9 is very similar to that of conformer *a*.

Table 8. Fragment Ions for Conformer *a* and Their Relative Probabilities[a]

	Temperature (K)				
m/*z*	1600	1750	1875	2000	2250
916.2				25	
900.2			26.7		
890.2	42.8	9.5	60		60
875.2[b]	42.8		66.6	42	
875.2[c]	28.6				
874.2	28.6	23.8	20	42	
873.2		19	100	58	40
872.2			13.3		
861.2		9.5		25	
840.2					40
837.2		19	40		40
821.2		19	20	25	20
811.2				42	
766.1	100	100	73.3	100	
764.1				42	
755.2			46.6		
738.1				42	40
727.1		9.5			60
723.1	14.3	9.5	46.6	100	100
707.1					40
693.1			33.3		
681.1					40
678.1				25	60
663.1			20		
658.1				50	40
636.1					40
601.1		9.5		25	40
587.1					40
558.1					40
541.1					60
421.0					40
393.1					40

[a]Results of the PM7 direct dynamics simulations. The percentage of the most probable ion is given as 100%. Only ions with a yield greater than 2% are listed. [b]Loss of (CONH). [c]Loss of $(COCH_3)$.

For gas phase CID mass spectra of peptides, it has been reported[83] that the most thermodynamically and kinetically favored mechanism involves loss of (H_2O+CO). Loss of CO, CH_2O_2, and the iminium ion $[CH_2{=}NH_2]^+$ is also observed in many amino acid systems.[83−89] For the present study, the majority of the *m*/*z* values involve loss of a small molecule as described above.

III.C. Direct Dynamics Simulations for Conformer a with MNDO/d. To compare the above PM7 results with those for another semiempirical electronic structure theory, 100 direct dynamics trajectories were calculated for conformer *a* at 2000 K for 10 ps using MNDO/d. The structure was first optimized using MNDO/d. Although, as shown in Table 1, MNDO/d predicts a similar energy trend for three conformers as found with PM7, there are differences in the MNDO/d and PM7 optimized structures for *a*. As discussed in section II.B, PM7 gives a structure in good agreement with experiment. Most notably, MNDO/d predicts the metal cation−π distance to be 2.6 Å longer than for PM7. This was probably the reason the

DOI: 10.1021/acs.jpca.9b05218
J. Phys. Chem. A 2019, 123, 6868−6885

Table 9. Fragment Ions for Conformers *b* and *c* and Their Relative Probabilities[a]

conformer *b*			conformer *c*	
m/*z*	2000 K[b]	2250 K	*m*/*z*	2000 K
890.2	33.3	42	874.2	83
875.2	41.7	33	837.2	33
874.2		25	766.1	100
873.2	33.3	25	723.1	50
837.2	100	100		
821.2	25			
811.2		25		
781.1	33.3	42		
766.1	83.3	83		
738.1	50	25		
723.1	25			
710.1		25		
679.1	41.7	25		
667.1		33		
601.1	25	25		
618.1		25		
464.0	33.3	33		

[a] Results of the PM7 direct dynamics simulations. The percentage of the most probable ion is given as 100%. Only ions with more than 2% of the total yield are included. [b] Temperature in Kelvin.

most important MNDO/d pathway was loss of (CH_2+PhOH) with *m*/*z* 811.2. MNDO/d overestimates the Zn−S bond strength, as compared to PM7, and this bond broke in none of the MNDO/d trajectories. There are only three pathways using MNDO/d, forming *m*/*z* 811.2, 766.1 ($([x_6+\ \mathrm{Zn(II)}]^-)$), and 658.1 ($([x_6-(CH_2+PhOH)+\mathrm{Zn(II)}]^-)$). As discussed in section IV, PM7 gives simulation results in qualitative agreement with experiment, while the MNDO/d results are in disagreement with experiment.

III.D. Thermal Unimolecular Rate Constants and Arrhenius Parameters. As discussed in section II.D, thermal unimolecular rate constants were determined for the conformers by plotting $\ln[N(t)/N(0)]$ versus time t, where $N(0)$ is the initial number of conformers for the simulation at $t = 0$ and $N(t)$ is the number of conformers remaining at t without fragmentation. An illustration of this analysis is shown in Figure 6 for conformer *a* at 1875 K. The thermal unimolecular rate constant $k(T)$ is found from the slope of this plot and this analysis was done for conformers *a*, *b*, and *c* for the different simulation temperatures. The resulting rate constants are listed in Table 10. The rate constants for conformers *a* and *b* are statistically the same, and there is an indication that the rate constant for conformer *c* may be somewhat smaller.

If the rate constants are represented by the Arrhenius equation, $k(T) = A\ \exp(-E_a/RT)$, the Arrhenius parameters may be determined from a plot of $\ln k(T)$ versus $1/T$. This analysis is shown in Figure 7 for conformer *a*, and the resulting Arrhenius parameters are $A = 4.5 \pm 2.1 \times 10^{14}\ \mathrm{s}^{-1}$ and $E_a = 31.9 \pm 1.8$ kcal/mol. For conformer *b*, the rate constants $k(T)$ for 2000 and 2250 K may be used to determine the Arrhenius parameters $A = 2.6 \pm 1.2 \times 10^{15}\ \mathrm{s}^{-1}$ and $E_a = 40.0 \pm 1.8$ kcal/mol. The A-factor for conformer *b* is ∼5 times larger than that for *a*. The larger E_a for *b* is consistent with the deeper potential energy minimum for *b* as compared to *a*, that is, see Table 1.

The rate constant $k_i(T)$ for an individual fragmentation pathway is given by $k_i(T) = p_i(T)k(T)$, where $p_i(T)$ is the probability for the pathway. For pathways 1 and 2 of conformer *a*, there was a sufficient number of fragmenting trajectories to find their $p_i(T)$. Figure 7 shows the plot of the natural logarithm of the rate constants $k_i(T)$ versus $1/T$ for pathways 1 and 2. The resulting Arrhenius parameters are $A = 5.9 \pm 5.4 \times 10^{13}\ \mathrm{s}^{-1}$ and $E_a = 35.8 \pm 3.6$ kcal/mol for pathway 1. For pathway 2, they are $A = 2.0 \pm 0.6 \times 10^{14}\ \mathrm{s}^{-1}$ and $E_a = 41.6 \pm 2.4$ kcal/mol.

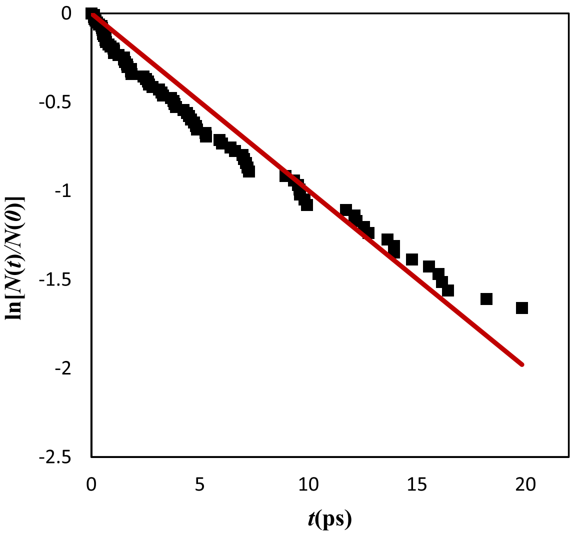

Figure 6. Plot of $\ln[N(t)/N(0)]$ versus t (ps) for conformer *a* at 1875 K.

Table 10. Thermal Rate Constants for Fragmentation of the Different $[\mathrm{amb}_5-3\mathrm{H}+\mathrm{Zn(II)}]^-$ Conformers[a]

	Conformer		
T (*K*)	*a*	*b*	*c*
1600	$1.31 \pm 0.48 \times 10^{10}$		
1750	$4.92 \pm 0.29 \times 10^{10}$		
1875	$9.97 \pm 0.22 \times 10^{10}$		
2000	$1.08 \pm 0.25 \times 10^{11}$	$1.10 \pm 0.23 \times 10^{11}$	$8.65 \pm 0.39 \times 10^{10}$
2250	$3.64 \pm 0.21 \times 10^{11}$	$3.33 \pm 0.20 \times 10^{11}$	

[a] Rate constants are in unit of s^{-1}.

There are two simulation *A*-factors for pathways 1 and 2, which involve C−C homolytic bond dissociation—3 orders of magnitude smaller than A-factors for C−C bond dissociation in alkanes.[90] The different *A*-factors for these C−C bond dissociations may be explained by the TST expression for the *A*-factor, and differences in the dynamics for alkane C−C bond dissociation and the C−C bond dissociations studied here. The TST *A*-factor is given by

$$A_{\mathrm{TST}} = \left({k_BT}/{h}\right)\exp\left(1 + {\Delta S^{\ddagger}}/{R}\right) \tag{3}$$

where k_B is Boltzmann's constant, h is Planck's constant, R is the gas law constant, and $\Delta S^{\ddagger}$ is the entropy of activation. At 2000 K, k_BT/h is $4.2 \times 10^{13}\ \mathrm{s}^{-1}$, which is similar to the A-factor for pathway 1 and only 5 times smaller than the A-factor for pathway 2. Thus, $\Delta S^{\ddagger}$ is quite small for the current C−C dissociations. In contrast, for an alkane C−C bond dissociation, with an A-factor 10^3 times larger than that for pathway 1, $\Delta S^{\ddagger} = 13.7$ cal/mol/K. For alkane C−C bond dissociations, for example, $C_4H_{10} \rightarrow 2C_2H_5$, vibrational motions of the alkane transform into rotation and translation motions of the radical products, giving rise to a large $\Delta S^{\ddagger}$. This degrees of freedom transformation also occurs for $[\mathrm{amb}_5-3\mathrm{H}+\mathrm{Zn(II)}]^-$ dissociation but, as discussed below,

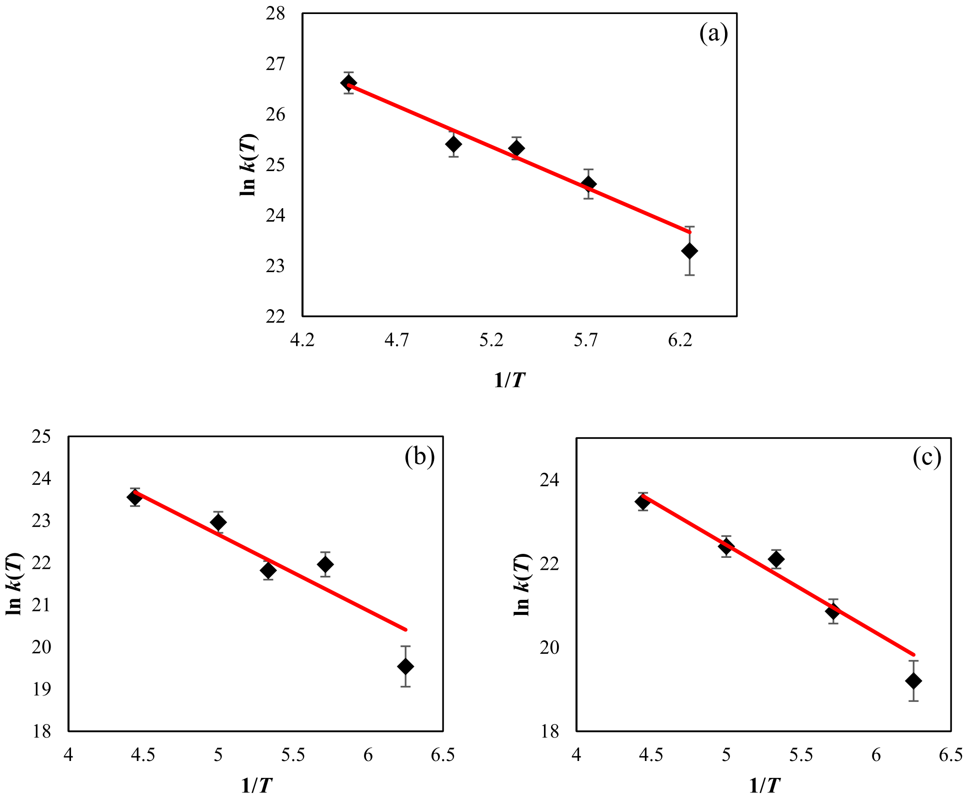

Figure 7. ln $k(T)$ versus $1/T$ (1×10^{-4} K^{-1}) for (a) total rate constant, (b) pathway 1, and (c) pathway 2 for conformer *a*. The fit was determined by including uncertainties in the $k(T)$ values.[75] The uncertainty in $k(T)$ is the 95% confidence interval standard error of the slope of $\ln[N(t)/N(0)]$ versus t for temperature T.

extensive hydrogen bonding also occurs within the dissociation products, tightening them and decreasing their entropy. This tightening effect does not occur for alkane C−C bond dissociation. The difference in A-factors for C−C bond dissociation for the biological ion studied here and alkanes, was also found in a previous study of the fragmentation of a doubly protonated tripeptide.[38]

Potential energy curves were calculated for the C−C bond dissociations of pathways 1 and 2. For one calculation the geometries of the fragment radicals were not optimized, as the C−C bond was stretched, and there was no barrier along the C−C dissociation potential energy curve, as expected for homolytic bond dissociation. However, when the geometries of the radical products were optimized, concomitantly with stretching of the C−C bond, a submerged barrier was found for each pathway as shown in Figure S3. This finding is more pronounced for pathway 2 than pathway 1. Apparently the submerged barrier arises from the interplay between the increase in potential energy with stretching of the C−C bond and release of potential energy upon optimization of the geometries of the radical products. Attempts were made to locate transition states for these barriers, but they were unsuccessful. Possibly, barriers for torsions and low frequency vibrations for the torsions and backbone vibrations make it difficult to optimize transition states for these barriers.

III.E. Differences between Arrhenius and Quantum Chemistry Dissociation Energies. The classical Arrhenius activation energy for a unimolecular reaction is equal to the difference between classical potential energies of the transition state (TS) and reactant.[38,74] Therefore, Arrhenius activation energy can be compared with barrier heights determined from electronic structure. For pathways 1 and 2, with submerged barriers, the TSs are expected to be variational transition states,[90−93] for which the TS is located at the maximum free energy of activation along the dissociation reaction coordinate. For the current simulations, there are pathways with a barrier that is not submerged, that involve concerted proton transfer and C−C bond breakage. However, their occurrence was not sufficient to determine their rate constants and Arrhenius parameters.

Arrhenius activation energies from direct dynamics simulations, as performed here, may be compared with potential energy barriers found from the electronic structure theory method used for the simulations.[38,74] For pathways 1 and 2, of the current PM7 direct dynamics simulations, it is of interest to compare the PM7 potential energy difference between the $[\mathrm{amb_5{-}3H{+}Zn(II)}]^-$ reactant, and unoptimized and optimized products, with the simulation activation energies. The simulation activation energy for pathway 1 is 35.8 ± 3.6 kcal/mol. In contrast, the PM7 potential energies for pathway 1 are 74.7 and 37.1 kcal/mol to form unoptimized and optimized products, respectively. For pathway 2 the simulation activation energy is 41.6 ± 2.4 kcal/mol, while the PM7 potential energies to form unoptimized and optimized products are 77.3 and 44.5 kcal/mol, respectively. For both pathways 1 and 2, the simulation activation energy is in good agreement with the PM7 potential energy between reactant and optimized products.

The simulation activation energies are much smaller than the PM7 potential energies for forming the unoptimized products. The same effect was found previously for bond dissociations of a doubly protonated tripeptide,[38] which was explained by extensive hydrogen bond stabilization of the dissociation

DOI: 10.1021/acs.jpca.9b05218
J. Phys. Chem. A 2019, 123, 6868−6885

products. As shown in Figure 8, such hydrogen bonding of the products is also found for the current C−C bond dissociations. However, for this study, there is also relieved steric strain for the optimized products. As a result of these effects, there is a large potential energy difference between the unoptimized and optimized products.

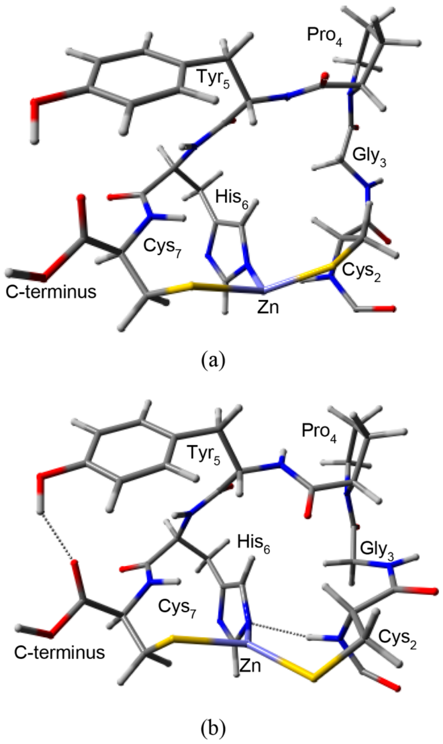

Figure 8. (a) Unoptimized and (b) optimized structures for a fragment of pathway 1 for conformer *a*. Hydrogen bonding stabilizes the optimized fragment, thus reducing the dissociation energy.

IV. COMPARISON OF FRAGMENTATION IONS FROM THE PM7 SIMULATIONS AND CID EXPERIMENTS

A comparison between the fragment ions observed in the PM7 simulations and the MS/MS CID experiments is given in Table 11. Conformer *c* gave very few ions and none of the ions which have a greater than 2% of the total yield differ from those for conformers *a* and *b*, and the results for conformer *c* are not included. Simulation results are given for conformer *a* at 1875, 2000, and 2250 K, and for conformer *b* at 2000 and 2250 K. Ions observed for conformer *a* at 1600 and 1750 K were also observed at the higher temperatures for this conformer. All of the 23 ions characterized in the MS/MS experiments are included. For the simulations, only ions with a probability 2% or greater than the total ion count are included, with the following proviso. If an ion with a lower probability is observed experimentally, it is included. There are three such ions; that is, m/z 770.2, 753.1, and 356.0, where m/z 770.2 is included to compare with the experiment m/z 769.2. Ions that are found only at one temperature and are not observed in the experiment are not included.

In the experiments, loss of one or two H_2S molecules was observed in six fragments. The ion m/z 884.2 was formed after loss of H_2S. The ions m/z 840.2, 822.2, 806.2, 705.1, and 480.1 involved the loss of one or two H_2S molecules along with other molecules. In the simulation, the only pathway in which H_2S loss was observed was pathway 10 in Figure 5, which also involved loss of CO_2. In the majority of the trajectories, for all three conformers, the Zn−S bond cleaved but did not produce separate fragments, including H_2S. As described above, one reason H_2S loss was not prevalent in the simulations was probably due to two factors; that is, the tetra-coordinated nature of the Zn ion and the short time periods for which the trajectories were integrated. As both thiol groups are deprotonated and bound to zinc, the loss of H_2S requires breaking a Zn−S bond followed by two proton transfers and cleavage of a H_2C−S bond.

There are six m/z values found both in the experiment and the simulations. The first common ion m/z 874.2 is for the loss of CO_2 and was found in the simulations from both conformers *a* and *b*. The m/z 872.2, 840.2, 636.1, and 356.0 were common ions produced by conformer *a*, with the m/z 872.2 and 840.2 for loss of $(CO+H_2O)$ and (CO_2+H_2S), respectively, with the simulation also exhibiting the loss of $(SCO+H_2O)$ at m/z 840.2. For m/z 636.1, both experiment and simulation produced the ion $[y_5+\mathrm{Zn(II)}]^-$, and as discussed in section III.A, simulation observed another channel with fragment ion $[y_6+\mathrm{Zn(II)}-(\mathrm{CONHCH_2+COOH})]^-$ for this m/z value. For m/z 356.0, the simulation exhibited $[a_2+y_1+\mathrm{Zn(II)}-(\mathrm{CH_2}+\mathrm{imi})]^-$. However, the experimental m/z 356.0 was determined to be $[b_3+\mathrm{Zn(II)}-(\mathrm{CH_3CHO})]^-$, which is related by loss of the acetyl group to the $[b_3+\mathrm{Zn(II)}]^-$ ion. A last related common ion was m/z 753.1 exhibited by the simulation of conformer *b* as fragment $[a_2+y_1+\mathrm{Zn(II)}]^-$. However, the experimental m/z 753.1 was determined to be $[b_6+\mathrm{Zn(II)}-(\mathrm{CH_3CHO})]^-$ related by the loss of the acetyl group to $[b_6+\mathrm{Zn(II)}]^-$. The $[b_6+\mathrm{Zn(II)}-(\mathrm{CH_3CHO})]^-$ and $[b_3+\mathrm{Zn(II)}-(\mathrm{CH_3CHO})]^-$ ions are related and their assignments were supported by further MS/MS/MS studies which showed $[b_3+\mathrm{Zn(II)}-(\mathrm{CH_3CHO})]^-$ was produced by dissociation of $[b_6+\mathrm{Zn(II)}-(\mathrm{CH_3CHO})]^-$, along with other product ions that were consistent with their assignments.

Both experiment and simulation predict the formation of $[y_6+\mathrm{Zn(II)}]^-$, $[a_6+\mathrm{Zn(II)}]^-$, and $[c_5+\mathrm{Zn(II)}]^-$ ions but they differ by a mass of 1. For the formation of $[y_6+\mathrm{Zn(II)}]^-$, the simulation predicts homolytic cleavage of the peptide bond, generating the radical $[y_6+\mathrm{Zn(II)}]^-$ at m/z 738.1 with a terminal $-\mathrm{NH}^\bullet$ group. However, the experiment observes the $[y_6+\mathrm{Zn(II)}]^-$ ion at m/z 739.1 and indicates a mechanism consistent with the mobile proton model, which has been extensively used to describe the ion fragmentation mechanisms.[94−98] In this model, a proton migrates to the amine of the peptide bond and initiates charge-directed cleavage of the peptide bond producing either b or y ions. For pathway 5 in Figure 4, this would require a proton to become mobile and transfer from the acetylated N-terminal fragment. This is possible because it would lead to the formation of a neutral charged oxazolone and the $[y_6+\mathrm{Zn(II)}]^-$ ion through analogous reactions described by bond-cleavage pathways of peptide ions lacking mobile protons as described by Bythell et al.[98] In this mechanism, the dissociation would be initiated by proton transfer from the amine group of the acetylated N-terminus to the neighboring amine group of the peptide bond. The peptide bond would dissociate through heterolytic cleavage with both electrons transferred to the amine group resulting in $[y_6+\mathrm{Zn(II)}]^-$ ion with a terminal $-\mathrm{NH_2}$ group, consistent with the mass observed at 739.1 m/z, accompanied by the formation of an oxazolone neutral product.

Differences between the simulations and experiments may be summarized as follows. For small molecule losses the simulations predict COOH loss via homolytic cleavage or

Table 11. Monoisotopic m/z Values of Ions Obtained from Simulations[a] for Conformers a and b and MS/MS CID Experiments[b]

	conformer a			conformer b	experiment		
m/z	1875[c]	2000	2250	2000	2250	MS/MS	fragment
890.2	√	-	√	√	√	-	$-(\mathrm{CO})$
884.2	-	-	-	-	-	√	$-(\mathrm{H_2S})$
875.2	√	√	-	√	√	-	$-(\mathrm{CONH})$
874.2	√	√	-	-	√	√	$-(\mathrm{CO_2})$
873.2	√	√	√	-	√	-	$-(\mathrm{COOH})$
872.2	√	-	-	-	-	√	$-(\mathrm{CO+H_2O})$
840.2	-	-	√	-	-	√	$-(\mathrm{SCO+H_2O})$ or $-(\mathrm{CO_2+H_2S})$
837.2	√	-	√	√	√	-	$-(\mathrm{CH_2+imi})$
822.2	-	-	-	-	-	√	$-(\mathrm{CO_2+H_2S+H_2O})$
821.2	√	√	√	√	-	-	$[a_3+x_3+\mathrm{Zn(II)}]^-$
811.2	-	√	-	-	√	-	$-(\mathrm{CH_2+PhOH})$
806.2	-	-	-	-	-	√	$-(\mathrm{CO_2+2H_2S})$
797.2	-	-	-	-	-	√	$[b_6+\mathrm{Zn(II)}]^-$
781.1	-	-	-	√	√	-	$[a_5+x_1+\mathrm{Zn(II)}]^-$
770.2	-	√	-	-	-	-	$[a_6+\mathrm{Zn(II)}]^-$
769.2	-	-	-	-	-	√	$[\mathrm{a}_6+\mathrm{Zn(II)}]^-$
766.1	√	√	-	√	√	-	$[x_6+\mathrm{Zn(II)}]^-$
753.1	-	-	-	√	√	√	$[y_1+a_5+\mathrm{Zn(II)}]^-$ and $[b_6+\mathrm{Zn(II)}\text{-}(\mathrm{CH_3COH})]^-$[d]
739.1	-	-	-	-	-	√	$[y_6+\mathrm{Zn(II)}]^-$
738.1	-	√	√	√	√	-	$[y_6+\mathrm{Zn(II)}]^-$ or $[x_6+\mathrm{Zn(II)}\text{-}(\mathrm{CO})]^-$
723.1	√	√	√	√	-	-	$[z_6+\mathrm{Zn(II)}]^-$
705.1	-	-	-	-	-	√	$[y_6+\mathrm{Zn(II)}-(\mathrm{H_2S})]^-$
679.1	-	-	-	√	√	-	$[z_6+\mathrm{Zn(II)}-(\mathrm{CO_2})]^-$
678.1	-	√	√	-	-	-	$[z_6+\mathrm{Zn(II)}-(\mathrm{COOH})]^-$ or $[c_5+\mathrm{Zn(II)}]^-$
677.1	-	-	-	-	-	√	$[c_5+\mathrm{Zn(II)}]^-$
660.1	-	-	-	-	-	√	$[b_5+\mathrm{Zn(II)}]^-$
658.1	-	√	√	-	-	-	$[b_3+y_2+\mathrm{Zn(II)}]^-$ or $[a_3+x_2+\mathrm{Zn(II)}]^-$
636.1	-	-	√	-	-	√	$[y_5+\mathrm{Zn(II)}]^-$
601.1	-	√	√	√	√	-	$[a_2+x_2+\mathrm{Zn(II)}]^-$
579.1	-	-	-	-	-	√	$[y_4+\mathrm{Zn(II)}]^-$
535.1	-	-	-	-	-	√	$[y_4+\mathrm{Zn(II)}-(\mathrm{CO_2})]^-$
514.1	-	-	-	-	-	√	$[c_4+\mathrm{Zn(II)}]^-$
501.1	-	-	-	-	-	√	$[a_4+\mathrm{Zn(II)S}]^-$
480.1	-	-	-	-	-	√	$[c_4+\mathrm{Zn(II)}-(\mathrm{H_2S})]^-$
464.0	-	-	-	√	√	-	$[a_2+x_1+\mathrm{Zn(II)}]^-$
421.0	-	-	√	-	-	-	$[a_3+\mathrm{SCH_2}+\mathrm{Zn(II)}]^-$
400.0	-	-	-	-	-	√	$[b_3+\mathrm{Zn(II)}]^-$
356.0	-	-	√	-	-	√	$[a_2+y_1+\mathrm{Zn(II)}-(\mathrm{CH_2+imi})]^-$ and $[b_3+\mathrm{Zn(II)}-(\mathrm{CH_3COH})]^-$[d]
343.0	-	-	-	-	-	√	$[b_2+\mathrm{Zn(II)}]^-$
315.0	-	-	-	-	-	√	$[a_2+\mathrm{Zn(II)}]^-$

[a] For the simulations at 1875, 2000, and 2250 K only ions with a probability 2% or greater than the total ion count are included, with the following provisos. If an ion with a low probability for the 2000 and 2250 K simulations is observed experimentally, it is included. Whereas ions that are found only at one temperature and are not observed in the experiment are not included. [b] For experiment all the ions are listed. [c] Temperature in Kelvin. [d] Fragment ion predicted from the experimental MS/MS spectrum.

CO_2 loss, both from the C-terminus, and fragmentation of the backbone peptide bond resulting in the loss of CO. Experiment, however, primarily exhibits H_2S, $H_2S + CO_2$, and $2H_2S + CO_2$, although $H_2S + CO_2$ loss is also observed as a minor channel for the simulation of conformer a. This is in agreement with $H_2S + CO_2$ loss being commonly observed from MS/MS of negatively charged peptides which contain Cys at the C-terminus.[99,100] Experiment also produces CO_2 loss from the C-terminus. Both simulations and experiment exhibit formation of the $[a_6+\mathrm{Zn(II)}]^-$, $[c_5+\mathrm{Zn(II)}]^-$, and $[y_6+\mathrm{Zn(II)}]^-$ ions but with a mass difference of 1, with the simulation also predicting the related $[x_6+\mathrm{Zn(II)}]^-$ ion. For these products, the simulations predict homolytic cleavage and formation of two radical products, whereas, the m/z product ion from experiment is consistent with formation of nonradicals through the mobile proton reaction mechanism.[94−98] The simulations predict double or triple cleavages of the backbone with the Zn(II) retaining its binding sites to the 2His−2Cys, for example, $[a_3+x_3+\mathrm{Zn(II)}]^-$ and $[a_2+x_2+\mathrm{Zn(II)}]^-$, whereas experiment exhibits single cleavages of the backbone accompanied by cleavage of two of the Zn(II) binding sites, resulting in b- and y-type ions.

V. SUMMARY

Direct dynamics simulations, using PM7 semiempirical electronic structure theory, were performed to study fragmentation of the negative ion formed by Zn(II) binding to the triply deprotonated peptide, with sequence acetyl-$\mathrm{His_1}$-$\mathrm{Cys_2}$-$\mathrm{Gly_3}$-$\mathrm{Pro_4}$-$\mathrm{Tyr_5}$-$\mathrm{His_6}$-$\mathrm{Cys_7}$, and identified as $[\mathrm{amb_5}-3\mathrm{H}+\mathrm{Zn(II)}]^-$.

Tests showed that PM7 gives geometries and bond dissociation energies for model Zn(II) compounds in overall good agreement with the findings of CCSD(T) and DFT theories. Three conformers, identified as *a*, *b*, and *c*, were found for $[\text{amb}_5-3\text{H}+\text{Zn(II)}]^-$, with PM7 and DFT giving a similar structure for each conformer. The coordinating ligands for the conformers adopted a distorted tetrahedral structure around Zn(II) and included the two thiolate groups of the cysteines. For structure *a*, the other two ligands were the imidazole and imidazolate groups of the two histidines, giving a 2His-2Cys binding motif. For structure *b*, the ligands included two oxygens from the carbonyl group of Cys_2 and the C-terminus carboxylate group. Conformer *c* included the imidazole from His_1 and the oxygen from the C-terminus carboxylate. Each electronic structure method identified conformer *b* as the lowest in energy, whose peptide bonds are all trans apart from the *cis*-Gly-Pro bond. However, PM7 and DFT give different ordering of the energies for conformers *a* and *c*. For DFT, *c* is lower in energy, while *a* is lower for PM7. Structures for the conformers are affected by the charges on the atoms, the deprotonation sites of amb_5, and their hydrogen bonding. PM7 bond angles for conformers *a* and *c* agree with X-ray crystallographic studies.

The direct dynamics simulations are compared with multiple collision CID experiments, for which the negatively charged $[\text{amb}_5-3\text{H}+\text{Zn(II)}]^-$ ion undergoes about 700 collisions with neutral argon atoms before it fragments. Such multiple collisions are expected to result in statistical activation of the ion and, for the direct dynamics simulations reported here, statistical thermal activation of the ion was considered. Conformer *a* was randomly excited at temperatures of 1600, 1750, 1875, 2000, and 2250 K, conformer *b* at 2000 and 2250 K, and conformer *c* at 2000 K. As the temperature was increased, there were more dissociation pathways. For structure *a*, the number of primary dissociation pathways are 11, 14, 24, 70, and 71 at temperature of 1600, 1750, 1875, 2000, and 2250 K, respectively. However, there were only 6, 10, 13, 14, and 19 respective pathways for these temperatures that have a probability of 2% or more. For structure *b*, there were 67 pathways at 2000 K and 71 pathways at 2250 K. For structure *c*, 17 pathways were observed at 2000 K.

There are dynamical features common to all the dissociation mechanisms for the conformers. For most of the pathways, more than one bond was broken to generate fragments. A prominent component of the mechanisms is homolytic dissociation of a C−C bond and breaking a bond with the Zn(II) ion, generating a tricoordinated Zn(II) complex. For conformer *a* at 1600 and 1750 K the dominant fragment ion is $[x_6+\text{Zn(II)}]^-$ with m/z 766.1. At 1875 K the dominant ion has m/z 873.2, formed by elimination of COOH. At 2000 K the dominant ions have m/z of 766.1 and 723.1, the latter $[z_6+\text{Zn(II)}]^-$. At 2250 K the dominant ion is m/z 723.1. Similar ions, as for conformer *a*, are formed for the fragmentation of conformers *b* and *c*.

For all temperatures considered, the dissociation kinetics for conformers *a*, *b*, and *c* follow RRKM unimolecular dynamics, indicating the conformers are intrinsic RRKM molecules.[101] At each temperature, the rate constant $k(T)$ is the sum of rate constants for individual fragmentation pathways $k_i(T)$, a product of $k(T)$ and the probability of occurrence of pathway *i*. Arrhenius parameters were calculated for pathways 1 and 2, which involve C−C bond dissociation. The frequency factors and activation energies are smaller than those for homolytic dissociation of C−C bond in alkanes, due to the stabilization of the products as a result of increased hydrogen bonding. For both pathways 1 and 2, the simulation activation energy is in good agreement with the PM7 potential energy between reactant and optimized products. The former for pathways 1 and 2 are 35.8 ± 3.6 and 41.6 ± 2.4 kcal/mol, while the respective values for the latter are 37.1 and 44.5 kcal/mol.

The fragment ions formed in the simulations were compared with those formed in the CID experiments. At best, there is only qualitative agreement between the simulation and experimental results. The simulations predict double or triple cleavages of the backbone with the Zn(II) retaining its binding sites to the 2His−2Cys, for example, $[a_3+x_3+\text{Zn(II)}]^-$ and $[a_2+x_2+\text{Zn(II)}]^-$, whereas the experiment exhibits single cleavages of the backbone accompanied by cleavage of two of the Zn(II) binding sites, resulting in *b*- and *y*-type ions. Comparison of the simulation results for the three different conformers suggests that the fragmentation pattern of conformer *a* most closely matches experiment even though conformer *b* is energetically more stable. This zinc binding behavior is consistent with established zinc chemistry in large biomolecules,[12−15,28] with solvation, which would be the source of $[\text{amb}_5-3\text{H}+\text{Zn(II)}]^-$ in the ESI experiments.

One strength of the direct dynamics simulations reported here is that they identify the primary dissociation pathways for the biological ion, which are 71 each for conformers *a* and *b* at 2250 K and 17 for conformer *c* at 2000 K; a total of 159 pathways. These would be difficult to identify without a simulation as performed here or by use of a search algorithm to identify reaction mechanisms.[102] In future work, it would be of interest to determine transition state structures and potential energy barriers[103] for the important dissociation pathways found here for $[\text{amb}_5\text{-}3\text{H}+\text{Zn(II)}]^-$.

■ ASSOCIATED CONTENT

Ⓢ Supporting Information

The Supporting Information is available free of charge on the ACS Publications website at DOI: 10.1021/acs.jpca.9b05218.

> MS/MS CID spectrum, additional fragmentation pathways, potential energy curves for pathways 1 and 2, mathematical formulation employed to calculate the weighted linear regression and the uncertainties, mean absolute errors for Zn−ligand bond distances, and all the ions (m/z) and their corresponding fragments for three conformers at different temperatures (PDF)

■ AUTHOR INFORMATION

Corresponding Author

*E-mail: bill.hase@ttu.edu.

ORCID

Abdul Malik: 0000-0003-1765-437X
William L. Hase: 0000-0002-0560-5100

Notes

The authors declare no competing financial interest.

■ ACKNOWLEDGMENTS

The authors thank Dr. Carol L. Korzeniewski (Texas Tech University) for her valuable guidance in statistical analyses and Dr. Sandhiya Lakshmanan for discussions concerning electronic structure calculations. The research at Texas Tech University was supported by the Robert A. Welch Foundation under Grant No. D-0005. S.P. has a Research Assistant Professor position supported by TTU. The simulations at Texas Tech University were performed with the computer clusters Chemdynm of the

Hase Research Group and Quanah of the TTU High Performance Computing Center. The research at A&M-Commerce was supported by the National Science Foundation under grant 1764436 and the Welch Foundation under grant T-0014.

■ REFERENCES

(1) Andreini, C.; Banci, L.; Bertini, I.; Rosato, A. Counting the Zinc-Proteins Encoded in the Human Genome. *J. Proteome Res.* **2006**, *5* (1), 196−201.

(2) Sugarman, B. Zinc and Infection. *Clin. Infect. Dis.* **1983**, *5* (1), 137−147.

(3) Mccall, K. A.; Huang, C. C.; Fierke, C. A. Function and Mechanism of Zinc Metalloenzymes. *J. Nutr.* **2000**, *130* (5), 1437S−1446S.

(4) Ho, E.; Song, Y. Zinc and Prostatic Cancer. *Curr. Opin. Clin. Nutr. Metab. Care* **2009**, *12* (6), 640−645.

(5) Li, M.; Zhang, Y.; Liu, Z.; Bharadwaj, U.; Wang, H.; Wang, X.; Zhang, S.; Liuzzi, J. P.; Chang, S. M.; Cousins, R. J.; Fisher, W. E.; Brunicardi, F. C.; Logsdon, C. D.; Chen, C.; Yao, Q. Aberrant Expression of Zinc Transporter ZIP4 (SLC39A4) Significantly Contributes to Human Pancreatic Cancer Pathogenesis and Progression. *Proc. Natl. Acad. Sci. U. S. A.* **2007**, *104* (47), 18636−18641.

(6) Franklin, R. B.; Levy, B. A.; Zou, J.; Hanna, N.; Desouki, M. M.; Bagasra, O.; Johnson, L. A.; Costello, L. C. ZIP14 Zinc Transporter Downregulation and Zinc Depletion in the Development and Progression of Hepatocellular Cancer. *J. Gastrointest. Cancer* **2012**, *43* (2), 249−257.

(7) Kagara, N.; Tanaka, N.; Noguchi, S.; Hirano, T. Zinc and Its Transporter Zip10 are Involved in Invasive Behavior of Breast Cancer Cells. *Cancer Sci.* **2007**, *98* (5), 692−697.

(8) Kepp, K. P. Bioinorganic Chemistry of Alzheimer's Disease. *Chem. Rev.* **2012**, *112* (10), 5193−5239.

(9) Spevacek, A. R.; Evans, E. G.; Miller, J. L.; Meyer, H. C.; Pelton, J. G.; Millhauser, G. L. Zinc Drives a Tertiary Fold in the Prion Protein with Familial Disease Mutation Sites at the Interface. *Structure* **2013**, *21* (2), 236−246.

(10) Kenche, V. B.; Barnham, K. J. Alzheimer's Disease & Metals: Therapeutic Opportunities. *Br. J. Pharmacol.* **2011**, *163* (2), 211−219.

(11) Huang, X.; Cuajungco, M. P.; Atwood, C. S.; Moir, R. D.; Tanzi, R. E.; Bush, A. I. Alzheimer's Disease, *β*-Amyloid Protein and Zinc. *J. Nutr.* **2000**, *130*, 1488S−1492S.

(12) Krężel, A.; Maret, W. The Biological Inorganic Chemistry of Zinc Ions. *Arch. Biochem. Biophys.* **2016**, *611*, 3−19.

(13) Cai, L.; Li, X. K.; Song, Y.; Cherian, M. Essentiality, Toxicology and Chelation Therapy of Zinc and Copper. *Curr. Med. Chem.* **2005**, *12* (23), 2753−2763.

(14) Pace, N.; Weerapana, E. Zinc-Binding Cysteines: Diverse Functions and Structural Motifs. *Biomolecules* **2014**, *4* (2), 419−434.

(15) Razin, S. V.; Borunova, V. V.; Maksimenko, O. G.; Kantidze, O. L. Cys_2His_2 Zinc Finger Protein Family: Classification, Functions, and Major Members. *Biochemistry (Moscow)* **2012**, *77* (3), 217−226.

(16) Sesham, R.; Choi, D.; Balaji, A.; Cheruku, S.; Ravichetti, C.; Alshahrani, A. A.; Nasani, M.; Angel, L. A. The pH Dependent Cu(II) and Zn(II) Binding Behavior of an Analog Methanobactin Peptide. *Eur. J. Mass Spectrom.* **2013**, *19* (6), 463−473.

(17) McCabe, J. W.; Vangala, R.; Angel, L. A. Binding Selectivity of Methanobactin from *Methylosinus trichosporium* OB3b for Copper(I), Silver(I), Zinc(II), Nickel(II), Cobalt(II), Manganese(II), Lead(II), and Iron(II). *J. Am. Soc. Mass Spectrom.* **2017**, *28*, 2588−2601.

(18) Martin, E. M.; Kondrat, F. D. L.; Stewart, A. J.; Scrivens, J. H.; Sadler, P. J.; Blindauer, C. A. Native Electrospray Mass Spectrometry Approaches to Probe the Interaction between Zinc and an Anti-Angiogenic Peptide from Histidine-Rich Glycoprotein. *Sci. Rep.* **2018**, *8* (1), 8646.

(19) Wyttenbach, T.; Liu, D.; Bowers, M. T. Interactions of the Hormone Oxytocin with Divalent Metal Ions. *J. Am. Chem. Soc.* **2008**, *130* (18), 5993−6000.

(20) Fuller, D. R.; Glover, M. S.; Pierson, N. A.; Kim, D.; Russell, D. H.; Clemmer, D. E. Cis→Trans Isomerization of Pro(7) in Oxytocin Regulates Zn(2+) Binding. *J. Am. Soc. Mass Spectrom.* **2016**, *27* (8), 1376−1382.

(21) Berezovskaya, Y.; Armstrong, C. T.; Boyle, A. L.; Porrini, M.; Woolfson, D. N.; Barran, P. E. Metal Binding to a Zinc-Finger Peptide: a Comparison between Solution and the Gas Phase. *Chem. Commun.* **2011**, *47* (1), 412−414.

(22) Berezovskaya, Y.; Porrini, M.; Nortcliffe, C.; Barran, P. E. The Use of Ion Mobility Mass Spectrometry to Assist Protein Design: a Case Study on Zinc Finger Fold versus Coiled Coil Interactions. *Analyst* **2015**, *140* (8), 2847−2856.

(23) Utley, B.; Angel, L. A. Effects of Transition Metal Ion Identity and Π-Cation Interactions in Metal-bis(peptide) Complexes Containing Phenylalanine. *Eur. J. Mass Spectrom.* **2010**, *16* (6), 631−643.

(24) Giganti, V. G.; Kundoor, S.; Best, W. A.; Angel, L. A. Ion Mobility-Mass Spectrometry Study of Folded Ubiquitin Conformers Induced by Treatment with cis-$Pd(en)(H_2O)_2^{2+}$. *J. Am. Soc. Mass Spectrom.* **2011**, *22* (2), 300−309.

(25) Raja, U. K. B.; Injeti, S.; Culver, T.; McCabe, J. W.; Angel, L. A. Probing the Stability of Insulin Oligomers Using Electrospray Ionization Ion Mobility Mass Spectrometry. *Eur. J. Mass Spectrom.* **2015**, *21* (6), 759−774.

(26) Glover, M. S.; Dilger, J. M.; Zhu, F.; Clemmer, D. E. The Binding of Ca^{2+}, Co^{2+}, Ni^{2+}, Cu^{2+}, and Zn^{2+} Cations to Angiotensin I Determined by Mass Spectrometry Based Techniques. *Int. J. Mass Spectrom.* **2013**, *354−355*, 318−325.

(27) Wagoner, S. M.; Deeconda, M.; Cumpian, K. L.; Ortiz, R.; Chinthala, S.; Angel, L. A. The Multiple Conformational Charge States of Zinc(II) Coordination by 2His-2Cys Oligopeptide Investigated by Ion Mobility-Mass Spectrometry, Density Functional Theory and Theoretical Collision Cross Sections. *J. Mass Spectrom.* **2016**, *51* (12), 1120−1129.

(28) Klug, A. The Discovery of Zinc Fingers and Their Applications in Gene Regulation and Genome Manipulation. *Annu. Rev. Biochem.* **2010**, *79*, 213−231.

(29) Zhou, L.; Li, S.; Su, Y.; Yi, X.; Zheng, A.; Deng, F. Interaction between Histidine and Zn(II) Metal Ions over a Wide PH as Revealed by Solid-State NMR Spectroscopy and DFT Calculations. *J. Phys. Chem. B* **2013**, *117* (30), 8954−8965.

(30) Yang, L.; Sun, R.; Hase, W. L. Use of Direct Dynamics Simulations to Determine Unimolecular Reaction Paths and Arrhenius Parameters for Large Molecules. *J. Chem. Theory Comput.* **2011**, *7*, 3478−3483.

(31) Kolakkandy, S.; Paul, A. K.; Pratihar, S.; Kohale, S. C.; Barnes, G. L.; Wang, H.; Hase, W. L. Energy and Temperature Dependent Dissociation of the $Na^+(benzene)_{1,2}$ Clusters. Importance of Anharmonicity. *J. Chem. Phys.* **2015**, *142* (4), No. 044306.

(32) Chen, L. X.; Gao, Y. Q.; Russell, D. H. How Alkali Metal Ion Binding alters the Conformation Preferences of Gramicidin A: A Molecular Dynamics and Ion Mobility Study. *J. Phys. Chem. A* **2012**, *116* (1), 689−696.

(33) Meroueh, S. O.; Wang, Y.; Hase, W. L. Direct Dynamics Simulations of Collision- and Surface-Induced Dissociation of N-Protonated Glycine. Shattering Fragmentation. *J. Phys. Chem. A* **2002**, *106*, 9983−9992.

(34) Wang, Y.; Hase, W. L.; Song, K. Direct Dynamics Study of N-Protonated Diglycine Surface-Induced Dissociation. Influence of Collision Energy. *J. Am. Soc. Mass Spectrom.* **2003**, *14*, 1402−1412.

(35) Park, K.; Deb, B.; Song, K.; Hase, W. L. Importance of Shattering Fragmentation in the Surface-Induced Dissociation of Protonated Octaglycine. *J. Am. Soc. Mass Spectrom.* **2009**, *20*, 939−948 (Julia Laskin Special Issue). .

(36) Barnes, G. L.; Hase, W. L. Energy Transfer, Unfolding, and Fragmentation Dynamics in Collisions of N-Protonated Octaglycine with an H-SAM Surface. *J. Am. Chem. Soc.* **2009**, *131*, 17185−17193.

(37) Barnes, G. L.; Young, K.; Yang, L.; Hase, W. L. Fragmentation and Reactivity in Collisions of Protonated Diglycine with Chemically

Modified Perfluorinated Alkylthiolate-Self-Assembled Monolayer Surfaces. *J. Chem. Phys.* **2011**, *134*, 094106.

(38) Homayoon, Z.; Pratihar, S.; Dratz, E.; Snider, R.; Spezia, R.; Barnes, G. L.; Macaluso, V.; Martin-Somer, A.; Hase, W. L. Model Simulations of the Thermal Dissociation of the TIK$(H^+)_2$ Tripeptide: Mechanisms and Kinetic Parameters. *J. Phys. Chem. A* **2016**, *120*, 8211−8227.

(39) Spezia, R.; Martin-Somer, A.; Macaluso, V.; Homayoon, Z.; Pratihar, S.; Hase, W. L. L. Unimolecular Dissociation of Peptides: Statistical vs. Non-statistical Fragmentation Mechanisms and Time Scales. *Faraday Discuss.* **2016**, *195*, 599−618.

(40) Homayoon, Z.; Macaluso, V.; Martin-Somer, A.; Muniz, M. C. N. B.; Borges, I.; Hase, W. L.; Spezia, R. Chemical Dynamics Simulations of CID of Peptide Ions: Comparisons between TIK$(H^+)_2$ and TLK$(H^+)_2$ Fragmentation Dynamics, and with Thermal Simulations. *Phys. Chem. Chem. Phys.* **2018**, *20*, 3614−3629.

(41) Martin-Somer, A.; Martens, J.; Grzetic, J.; Hase, W. L.; Oomens, J.; Spezia, R. Unimolecular Fragmentation of Deprotonated Diproline $[Pro_2\text{-}H]^-$ Studied by Chemical Dynamics Simulations and IRMPD Spectroscopy. *J. Phys. Chem. A* **2018**, *122* (10), 2612−2625.

(42) Macaluso, V.; Homayoon, Z.; Spezia, R.; Hase, W. L. Threshold for Shattering Fragmentation in Collision-Induced Dissociation of the Doubly Protonated Tripeptide TIK$(H^+)_2$. *Phys. Chem. Chem. Phys.* **2018**, *20*, 19744−19749.

(43) Amin, E. A.; Truhlar, D. G. Zn Coordination Chemistry: Development of Benchmark Suites for Geometries, Dipole Moments, and Bond Dissociation Energies and their use to Test and Validate Density Functionals and Molecular Orbital Theory. *J. Chem. Theory Comput.* **2008**, *4* (1), 75−85.

(44) Sorkin, A.; Truhlar, D. G.; Amin, E. A. Energies, Geometries, and Charge Distributions of Zn Molecules, Clusters, and Biocenters from Coupled Cluster, Density Functional, and Neglect of Diatomic Differential Overlap Models. *J. Chem. Theory Comput.* **2009**, *5* (5), 1254−1265.

(45) Munzarová, M.; Kaupp, M. A Critical Validation of Density Functional and Coupled-Cluster Approaches for the Calculation of EPR Hyperfine Coupling Constants in Transition Metal Complexes. *J. Phys. Chem. A* **1999**, *103* (48), 9966−9983.

(46) Cramer, C. J.; Włoch, M.; Piecuch, P.; Puzzarini, C.; Gagliardi, L. Theoretical Models on the Cu_2O_2 Torture Track: Mechanistic Implications for Oxytyrosinase and Small-Molecule Analogues. *J. Phys. Chem. A* **2006**, *110* (5), 1991−2004.

(47) Stewart, J. J. P. Optimization of Parameters for Semiempirical Methods VI: More Modifications to the NDDO Approximations and Re-optimization of Parameters. *J. Mol. Model.* **2013**, *19* (1), 1−32.

(48) Hay, P. J.; Wadt, W. R. Ab Initio Effective Core Potentials for Molecular Calculations. Potentials for the Transition Metal Atoms Sc to Hg. *J. Chem. Phys.* **1985**, *82* (1), 270−283.

(49) Hay, P. J.; Wadt, W. R. Ab Initio Effective Core Potentials for Molecular Calculations. Potentials for K to Au Including the Outermost Core Orbitals. *J. Chem. Phys.* **1985**, *82* (1), 299−310.

(50) Hostaš, J.; Řezáč, J.; Hobza, P. On the Performance of the Semiempirical Quantum Mechanical PM6 and PM7Methods for Noncovalent Interactions. *Chem. Phys. Lett.* **2013**, *568*, 161−166.

(51) Hay, P. J. Gaussian Basis Sets for Molecular Calculations. The Representation of 3d Orbitals in Transition-Metal Atoms. *J. Chem. Phys.* **1977**, *66* (10), 4377−4384.

(52) Joseph, A. P.; Srinivasan, N.; de Brevern, A. G. Cis-trans Peptide Variations in Structurally Similar Proteins. *Amino Acids* **2012**, *43* (3), 1369−1381.

(53) Garcia-Pino, A.; Buts, L.; Wyns, L.; Loris, R. Interplay Between Metal Binding and cis/trans Isomerization in Legume Lectins: Structural and Thermodynamic Study of P. angolensis Lectin. *J. Mol. Biol.* **2006**, *361* (1), 153−167.

(54) Fuller, D. R.; Conant, C. R.; El-Baba, T. J.; Brown, C. J.; Woodall, D. W.; Russell, D. H.; Clemmer, D. E. Conformationally Regulated Peptide Bond Cleavage in Bradykinin. *J. Am. Chem. Soc.* **2018**, *140* (30), 9357−9360.

(55) Bouckaert, J.; Dewallef, Y.; Poortmans, F.; Wyns, L.; Loris, R. The Structural Features of Concanavalin A Governing Non-Proline Peptide Isomerization. *J. Biol. Chem.* **2000**, *275* (26), 19778−19787.

(56) Cheesman, C.; Freedman, R. B.; Ruddock, L. W. The Disassembly and Reassembly of Mutants of Escherichia Coli Heat-Labile Enterotoxin: Replacement of Proline 93 does not Abolish the Reassembly-Competent and Reassembly-Incompetent States. *Biochemistry* **2004**, *43* (6), 1618−1625.

(57) Guan, R. J.; Xiang, Y.; He, X. L.; Wang, C. G.; Wang, M.; Zhang, Y.; Sundberg, E. J.; Wang, D. C. Structural Mechanism Governing cis and trans Isomeric States and an Intramolecular Switch for cis/trans Isomerization of a Non-proline Peptide Bond Observed in Crystal Structures of Scorpion Toxins. *J. Mol. Biol.* **2004**, *341* (5), 1189−1204.

(58) He, X. L.; Li, H. M.; Zeng, Z. H.; Liu, X. Q.; Wang, M.; Wang, D. C. Crystal Structures of Two α-Like Scorpion Toxins: Non-proline cis Peptide Bonds and Implications for New Binding Site Selectivity on the Sodium Channel. *J. Mol. Biol.* **1999**, *292* (1), 125−135.

(59) Sakharov, D. V.; Lim, C. Zn Protein Simulations Including Charge Transfer and Local Polarization Effects. *J. Am. Chem. Soc.* **2005**, *127* (13), 4921−4929.

(60) Touw, W. G.; van Beusekom, B.; Evers, J. M. G.; Vriend, G.; Joosten, R. P. Validation and Correction of Zn−Cys$_x$His$_y$ Complexes. *Acta Crystallogr.* **2016**, *72* (10), 1110−1118.

(61) Elrod-Erickson, M.; Rould, M. A.; Nekludova, L.; Pabo, C. O. Zif268 Protein-DNA Complex Refined at 1.6 A: a Model System for Understanding Zinc Finger DNA Interactions. *Structure* **1996**, *4* (10), 1171−1180.

(62) Hu, X.; Hase, W. L.; Pirraglia, T. Vectorization of the General Monte Carlo Classical Trajectory Program VENUS. *J. Comput. Chem.* **1991**, *12*, 1014−1024.

(63) Hase, W. L.; Duchovic, R. J.; Hu, X.; Komornicki, A.; Lim, K. F.; Lu, D. H.; Peslherbe, G. H.; Swamy, K. N.; Vande Linde, S. R.; Varandas, A.; Wang, H.; Wolf, R. J. VENUS. A General Chemical Dynamics Computer Program. *QCPE Bull.* **1996**, *16*, 671.

(64) Stewart, J. P. MOPAC2012; Stewart Computational Chemistry: Colorado Springs, CO, HTTP://OpenMOPAC.net, 2012.

(65) Hase, W. L.; Buckowski, D. G. Monte Carlo Sampling of a Microcanonical Ensemble of Classical Harmonic Oscillators. *Chem. Phys. Lett.* **1980**, *74*, 284−286.

(66) Verlet, L. Computer "Experiments" on Classical Fluids. I. Thermodynamical Properties of Lennard−Jones Molecules. *Phys. Rev.* **1967**, *159*, 98−103.

(67) Schlier, C.; Seiter, A. High-order Symplectic Integration: An Assessment. *Comput. Phys. Commun.* **2000**, *130*, 176−189.

(68) Schlier, C.; Seiter, A. Integration of Classical Trajectories: A Case Study. *J. Phys. Chem. A* **1998**, *102*, 9399−9404.

(69) Hase, W.; Unimolecular, L. and Intramolecular Dynamics. Relationship to Potential Energy Surface Properties. *J. Phys. Chem.* **1986**, *90* (3), 365−374.

(70) Nesbitt, D. J.; Field, R. W. Vibrational Energy Flow in Highly Excited Molecules: Role of Intramolecular Vibrational Redistribution. *J. Phys. Chem.* **1996**, *100* (31), 12735−12756.

(71) Uzer, T.; Miller, W. H. Theories of Intramolecular Vibrational Energy Transfer. *Phys. Rep.* **1991**, *199* (2), 73−146.

(72) Oref, I.; Rabinovitch, B. S. Do Highly Excited Reactive Polyatomic Molecules Behave Ergodically? *Acc. Chem. Res.* **1979**, *12* (5), 166−175.

(73) Baer, T.; Hase, W. L. *Unimolecular Reaction Dynamics. Theory and Experiments*; Oxford: New York, 1996.

(74) Yang, L.; Sun, R.; Hase, W. L. Use of Direct Dynamics Simulations to Determine Unimolecular Reaction Paths and Arrhenius Parameters for Large Molecules. *J. Chem. Theory Comput.* **2011**, *7*, 3478−3483.

(75) Miller, J. N; Miller, J. C. *Statistics and Chemometrics for Analytical Chemistry*, 4th ed.; Prentice Hall: New York, 2000; pp 135−137.

(76) Lourderaj, U.; McAfee, J. L.; Hase, W. L. Potential Energy Surface and Unimolecular Dynamics of Stretched n-Butane. *J. Chem. Phys.* **2008**, *129*, No. 094701.

(77) Steinfeld, J. I.; Francisco, J. S.; Hase, W. L. *Chemical Kinetics and Dynamics*, 2nd ed.; Prentice-Hall: New York, 1999.

(78) Ma, X.; Paul, A. K.; Hase, W. L. Chemical Dynamics Simulations of Benzene Dimer Dissociation. *J. Phys. Chem. A* **2015**, *119*, 6631−6640.

(79) Gatland, I. R.; Thompson, W. J. A Weight-Watchers Guide to Least-Squares Fitting. *Comput. Phys.* **1993**, *7*, 280−285.

(80) Bevington, P. R.; Robinson, D. K. *Data Reduction and Error Analysis for the Physical Sciences*, 3rd ed.; McGraw Hill: New York, 2010.

(81) Roepstorff, P.; Fohlman, J. Proposal for a Common Nomenclature for Sequence Ions in Mass Spectra of Peptides. *Biomed. Mass Spectrom.* **1984**, *11*, 601.

(82) Liang, Y.; Neta, P.; Yang, X.; Stein, S. E. Collision-Induced Dissociation of Deprotonated Peptides. Relative Abundance of Side-Chain Neutral Losses, Residue-Specific Product Ions, and Comparison with Protonated Peptides. *J. Am. Soc. Mass Spectrom.* **2018**, *29* (3), 463−469.

(83) O'Hair, R. A. J.; Broughton, P. S.; Styles, M. L.; Frink, B. T.; Hadad, C. M. The Fragmentation Pathways of Protonated Glycine: A Computational Study. *J. Am. Soc. Mass Spectrom.* **2000**, *11*, 687−696.

(84) Laskin, J.; Denisov, E.; Futrell, J. A Comparative Study of Collision Induced and Surface-Induced Dissociation. 1. Fragmentation of Protonated Dialanine. *J. Am. Chem. Soc.* **2000**, *122*, 9703−9714.

(85) Abirami, S.; Xing, Y. M.; Tsang, C. W.; Ma, N. L. Theoretical Study of α/β-alanine and Their Protonated/Alkali Metal Cationized Complexes. *J. Phys. Chem. A* **2005**, *109*, 500−506.

(86) Tsang, C. W.; Harrison, A. G. Chemical Ionization of Amino Acids. *J. Am. Chem. Soc.* **1976**, *98*, 1301−1308.

(87) El Aribi, H.; Rodriquez, C. F.; Almeida, D. R. P.; Ling, Y.; Mak, W. W. N.; Hopkinson, A. C.; Siu, K. W. M. Elucidation of Fragmentation Mechanisms of Protonated Peptide Ions and their Products: A Case study on glycylglycylglycine using Density Functional Theory and Threshold Collision-Induced Dissociation. *J. Am. Chem. Soc.* **2003**, *125*, 9229−9236.

(88) Beranova, S.; Cai, J.; Wesdemiotis, C. Unimolecular Chemistry of Protonated Glycine and Its Neutralized Form in the Gas Phase. *J. Am. Chem. Soc.* **1995**, *117* (37), 9492−9501.

(89) Zhang, K.; Zimmerman, D. M.; Chung-Phillips, A.; Cassady, C. J. Experimental and Ab Initio Studies of the Gas-Phase Basicities of Polyglycines. *J. Am. Chem. Soc.* **1993**, *115*, 10812−10822.

(90) Hase, W. L. The Criterion of Minimum State Density in Unimolecular Rate Theory. An Application to Ethane Dissociation. *J. Chem. Phys.* **1976**, *64*, 2442−2449.

(91) Klippenstein, S. J. Variational Optimizations in the Rice−Ramsperger−Kassel−Marcus Theory Calculations for Unimolecular Dissociations with no Reverse Barrier. *J. Chem. Phys.* **1992**, *96*, 367−371.

(92) Wardlaw, D. M.; Marcus, R. A. On the Statistical Theory of Unimolecular Processes. *Adv. Chem. Phys.* **2007**, *70*, 231−264.

(93) Hase, W. L. Variational Unimolecular Rate Theory. *Acc. Chem. Res.* **1983**, *16*, 258−264.

(94) Dongre, A. R.; Jones, J. L.; Somogyi, A.; Wysocki, V. H. Influence of Peptide Composition, Gas-Phase Basicity, and Chemical Modification on Fragmentation Efficiency: Evidence for the Mobile Proton Model. *J. Am. Chem. Soc.* **1996**, *118*, 8365−8374.

(95) Gu, C.; Somogyi, A.; Wysocki, V. H.; Medzihradszky, K. F. Fragmentation of Protonated Oligopeptides XLDVLQ (X = L, H, K or R) by Surface Induced Dissociation: Additional Evidence for the 'Mobile Proton' Model. *Anal. Chim. Acta* **1999**, *397*, 247−256.

(96) Wysocki, V. H.; Tsaprailis, G.; Smith, L. L.; Breci, L. A. Mobile and Localized Protons: A Framework for Understanding Peptide Dissociation. *J. Mass Spectrom.* **2000**, *35*, 1399−1406.

(97) Boyd, R.; Somogyi, A. The Mobile Proton Hypothesis in Fragmentation of Protonated Peptides: A Perspective. *J. Am. Soc. Mass Spectrom.* **2010**, *21*, 1275−1278.

(98) Bythell, B. J.; Suhai, S.; Somogyi, A.; Paizs, B. Proton-Driven Amide Bond-Cleavage Pathways of Gas-Phase Peptide Ions Lacking Mobile Protons. *J. Am. Chem. Soc.* **2009**, *131*, 14057−14065.

(99) Bilusich, D.; Brinkworth, C. S.; McAnoy, A. M.; Bowie, J. H. The Fragmentations of [M-H]$^-$ Anions Derived from Underivatised Peptides. The Side-Chain Loss of H_2S from Cys. A Joint Experimental and Theoretical Study. *Rapid Commun. Mass Spectrom.* **2003**, *17*, 2488−2494.

(100) Bilusich, D.; Bowie, J. H. Fragmentations of (M−H)$^-$ Anions of Underivatised Peptides. Part 2: Characteristic Cleavages of Ser and Cys and of Disulfides and other Post-Translational Modifications, Together with some Unusual Internal Processes. *Mass Spectrom. Rev.* **2009**, *28* (1), 20−34.

(101) Bunker, D. L.; Hase, W. L. On Non-RRKM Unimolecular Kinetics: Molecules in General and CH_3NC in Particular. *J. Chem. Phys.* **1973**, *59*, 4621−4632.

(102) Martínez-Núñez, E. An Automated Method to Find Transition States using Chemical Dynamics Simulations. *J. Comput. Chem.* **2015**, *36*, 222−234.

(103) Rossich Molina, E.; Salpin, J.-Y.; Spezia, R.; Martinez-Nunez, E. On the Gas Phase Fragmentation of Protonated Uracil: A Statistical Perspective. *Phys. Chem. Chem. Phys.* **2016**, *18*, 14980−14990.

DOI: 10.1021/acs.jpca.9b05218
J. Phys. Chem. A 2019, 123, 6868−6885